

# Self-organized oscillations of Leidenfrost drops

Xiaolei Ma<sup>†</sup>, Justin C. Burton

Department of Physics, Emory University, Atlanta, Georgia 30322, USA

(Received xx; revised xx; accepted xx)

In the Leidenfrost effect, a thin layer of evaporated vapor forms between a liquid and a hot solid. The complex interactions between the solid, liquid, and vapor phases can lead to rich dynamics even in a single Leidenfrost drop. Here we investigate the self-organized oscillations of Leidenfrost drops that are excited by a constant flow of evaporated vapor beneath the drop. We show that for small Leidenfrost drops, the frequency of a recently reported “breathing mode” (Caswell, *Phys. Rev. E*, vol. 90, 2014, 013014) can be explained by a simple balance of gravitational and surface tension forces. For large Leidenfrost drops, azimuthal star-shaped oscillations are observed. Our previous work showed how the coupling between the rapid evaporated vapor flow and the vapor-liquid interface excites the star oscillations (Ma *et al.*, *Phys. Rev. Fluids*, vol. 2, 2017, 031602). In our experiments, star-shaped oscillation modes of  $n = 2$  to 13 are observed in different liquids, and the number of observed modes depends sensitively on the viscosity of the liquid. Here we expand on this work by directly comparing the oscillations with theoretical predictions, as well as show how the oscillations are initiated by a parametric forcing mechanism through pressure oscillations in the vapor layer. The pressure oscillations are driven by the capillary waves of a characteristic wavelength beneath the drop. These capillary waves can be generated by a large shear stress at the liquid-vapor interface due to the rapid flow of evaporated vapor. We also explore potential effects of thermal convection in the liquid. Although the measured Rayleigh number is significantly larger than the critical Rayleigh number, the frequency (wavelength) of the oscillations depends only on the capillary length of the liquid, and is independent of the drop radius and substrate temperature. Thus convection seems to play a minor role in Leidenfrost drop oscillations, which are mostly hydrodynamic in origin.

**Key words:**

---

## 1. Introduction

When a volatile liquid drop is deposited on a sufficiently hot solid, it can survive for minutes due to the presence of a thermally-insulating layer of evaporated vapor beneath the drop. In this levitated state, commonly known as the Leidenfrost regime (Leidenfrost 1756), the supporting vapor layer is maintained by the sustained evaporation of the liquid, and individual drops are free to undergo frictionless motion due to the absence of liquid-solid contact. The Leidenfrost effect can be easily observed by placing a water drop onto a hot pan over a cook stove in the kitchen, and has been the subject of numerous fundamental and applied studies due to the complex and rich interactions between the

<sup>†</sup> Email address for correspondence: xiaolei.ma@emory.edu

solid, liquid, and vapor phases (Qu er  2013). Examples include the evaporation dynamics and geometry of the drop (Burton *et al.* 2012; Biance *et al.* 2003; Myers & Charpin 2009; Pomeau *et al.* 2012; Xu & Qian 2013; Sobac *et al.* 2014; Hidalgo-Caballero *et al.* 2016; Maquet *et al.* 2016; Wong *et al.* 2017), the stability of the vapor-liquid interface (Duchemin *et al.* 2005; Lister *et al.* 2008; Snoeijer *et al.* 2009; Bouwhuis *et al.* 2013; Trinh *et al.* 2014; Raux *et al.* 2015; Maquet *et al.* 2015), hydrodynamic drag-reduction (Vakarelski *et al.* 2011, 2012, 2014), self-propulsion of droplets (Linke *et al.* 2006; Dupeux *et al.* 2011*b,a*; Lagubeau *et al.* 2011; Cousins *et al.* 2012; Li *et al.* 2016; Soto *et al.* 2016; Sobac *et al.* 2017), impact dynamics (Biance *et al.* 2006; Tran *et al.* 2012; Castanet *et al.* 2015; Shirota *et al.* 2016), green nanofabrication (Abdelaziz *et al.* 2013), chemical reactions (Bain *et al.* 2016), fuel combustion (Kadota *et al.* 2007), quenching process in metallurgy (Bernardin & Mudawar 1999), heat transfer (Talari *et al.* 2018; Shahriari *et al.* 2014), directional transport (Li *et al.* 2016), soft heat engines (Waitukaitis *et al.* 2017) and thermal control of nuclear reactors (Van Dam 1992).

In many of these examples, transient and self-sustained capillary oscillations play an important role in the dynamics. The interplay between gravity, the flow of vapor beneath the drop, and the liquid surface tension can lead to both small- and large-amplitude oscillations with very little damping. An understanding of these detailed interactions is crucial for the stability of the vapor layer, the failure of which can lead to explosive boiling upon contact with the hot surface. However, the excitation mechanism of these oscillations is complicated by the presence of both hydrodynamic and thermal effects, for example, rapidly-flowing vapor can cause a strong shear stress at the liquid-vapor interface, and temperature gradients in the liquid can lead to convective and Marangoni forces. Here we focus on capillary oscillations in individual Leidenfrost drops, where the shape is mostly determined by the competition between the gravity and surface tension, as measured by the relative size of the drop with respect to the capillary length,  $l_c \equiv \sqrt{\gamma/\rho_l g}$ , where  $\gamma$  and  $\rho_l$  denote the surface tension and density of the liquid, and  $g$  is the acceleration due to gravity. For drops with radius  $R < l_c$ , surface tension forces are dominant, and the drop shape is essentially spherical except for a vanishingly small flat region near the solid surface (Burton *et al.* 2012). Caswell (2014) identified a planar vibrational mode (“breathing” mode) in the neck region of the drop closest to the solid substrate. The oscillation frequencies were found to obey a power law that is not consistent with a general three-dimensional dispersion relation for capillary waves (Rayleigh 1879). In this paper, we provide an analytical expression for the breathing mode using a simple model based on gravity and surface tension which shows excellent agreement with the experimental data.

Large Leidenfrost drops form liquid puddles whose thickness is approximately  $2l_c$ . These puddles are known to spontaneously form large-amplitude, star-shaped oscillations (Holter & Glasscock 1952; Adachi & Takaki 1984; Strier *et al.* 2000; Snezhko *et al.* 2008; Strier *et al.* 2000; Ma *et al.* 2015, 2017). Similar oscillations have been observed in large drops on periodically-shaken, hydrophobic surfaces (Noblin *et al.* 2005, 2009), drops levitated by an underlying airflow (Bouwhuis *et al.* 2013), and drops excited by an external acoustic or electric field (Shen *et al.* 2010*a,b*; Mampallil *et al.* 2013). In studies where the frequency of external forcing is prescribed, the oscillations are excited by a parametric mechanism (Brunet & Snoeijer 2011). The external forcing leads to variations in the drop radius with time. Since the drop radius appears in the dispersion relation for azimuthal, star-shaped oscillations, the evolution of the oscillation amplitude obeys an equation similar to the Mathieu equation. For Leidenfrost drops, however, the mechanism is less clear since there is no prescribed frequency, and the star oscillations are excited and sustained through the heat input and resulting evaporation of the liquid. It has been

suggested that the star oscillations may result from modulations of the surface tension of the liquid due to temperature variations (Adachi & Takaki 1984; Takaki & Adachi 1985; Tokugawa & Takaki 1994), or perhaps due to convective patterns (Snezhko *et al.* 2008; Strier *et al.* 2000). However, (Bouwhuis *et al.* 2013) observed star-shaped oscillations in drops which are supported by an external, steady air flow, suggest that a hydrodynamic coupling between the gas flow and liquid interface initiates the oscillations.

Given the importance of the Leidenfrost effect in basic fluid and thermal transport, or the numerous practical applications, we know surprisingly little about the coupling between the evaporated vapor flow and vapor-liquid interface that lead to rich dynamical phenomena. Here we explore this coupling by investigating the self-organized, star-shaped oscillations of Leidenfrost drops using six different liquids: water, liquid N<sub>2</sub>, ethanol, methanol, acetone and isopropanol. The liquid drops were levitated on curved surfaces in order to suppress the Rayleigh-Taylor instability, and star-shaped oscillation modes with  $n = 2$  to 13 lobes along the drop periphery were observed. The number of observed modes depended sensitively on the liquid viscosity, whereas the oscillation frequency (wavelength) depended only on the capillary length but not the mode number, substrate temperature, or drop size. Accompanying pressure measurements in the center of the vapor layer indicate that the pressure variation frequency was approximately twice that the drop oscillation frequency for all of the observed modes, consistent with a parametric forcing mechanism. We show that the pressure oscillations are driven by capillary waves of a characteristic wavelength beneath the drop traveling from the drop center to the edge, and such capillary waves can be generated by a strong shear stress at the liquid-vapor interface. Additionally, we find that although thermal convection is expected to be quite strong, the robust frequency (wavelength) of star oscillations is only weakly affected by varying either the substrate or environmental temperature, suggesting that star-shaped oscillations of Leidenfrost drops are hydrodynamic in origin.

## 2. Experiment

In the experiment, blocks of engineering 6061 aluminum alloy with dimensions of  $\sim 7.6 \text{ cm} \times 7.6 \text{ cm} \times 2.5 \text{ cm}$  were used as substrates. Resistive heaters were embedded with high-temperature cement into the aluminum to control the substrate temperature,  $T_s$ . Six different liquids were used as Leidenfrost drops: deionized water, liquid nitrogen (liquid N<sub>2</sub>), ethanol, methanol, acetone, and isopropyl alcohol (isopropanol). The relevant liquid properties at the boiling point,  $T_b$ , such as the surface tension  $\gamma$ , density  $\rho_l$ , dynamic viscosity  $\eta_l$ , and capillary length  $l_c$ , are listed in table 1. The substrates were heated to different temperatures based on  $T_b$  for each liquid. For water, the temperature of the substrate was set from 523 K to 773 K, for ethanol, methanol, acetone, and isopropanol the temperature of the substrate was set to 523 K, whereas the substrate for liquid N<sub>2</sub> was not heated due to its extremely low  $T_b$ .

The upper surfaces of the substrates were machined into a concave, spherical shape in order to suppress the buoyancy-driven Rayleigh-Taylor instability at the vapor-liquid interface and keep the drops stationary (Snoeijer *et al.* 2009; Quéré 2013; Trinh *et al.* 2014). After machining, the roughness of the surface was inspected using an optical microscopy with  $50\times$  magnification. By changing the focus, we determined that over a  $250 \mu\text{m} \times 250 \mu\text{m}$  surface area, the peak-to-peak roughness was less than  $10 \mu\text{m}$ , and often much smaller than this value. The curved surfaces for different liquids were designed to satisfy  $l_c/R_s = 0.03$ , where  $R_s$  is the radius of curvature of the surface whose top and cross-sectional views are schematically shown in figures 1(a) and 1(b), respectively. Following this principle, we fabricated three types of curved substrates, i.e. one for water,

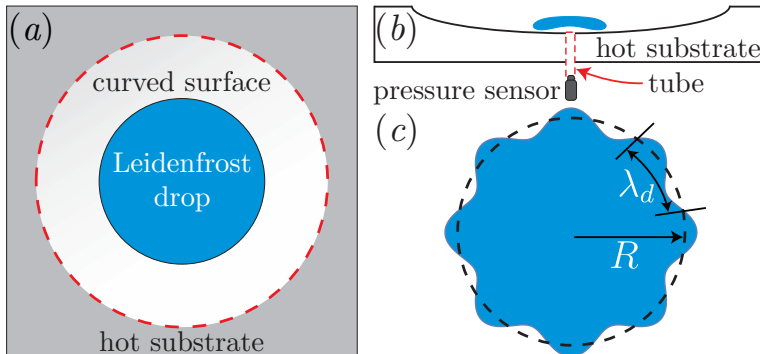


FIGURE 1. (Color online) Schematics of the experimental setup and star-shaped oscillation pattern. (a) Top-down view of the substrate whose upper surface is milled into a bowl shape enclosed by the dashed red circle. (b) Cross-sectional view of the substrate. (c) Star-shaped oscillation pattern of a Leidenfrost drop showing the standing wave along the drop periphery, which obeys  $2\pi R = n\lambda_d$ , where  $R$  is the drop radius,  $n$  is the number of lobes, and  $\lambda_d$  is the wavelength of the standing wave.

liquid	$T_b$	$\gamma$	$\rho_l$	$\eta_l$	$l_c$	$T_s$	Modes	$Re_l$
water	373	59.0	958	0.282	2.5	523-773	2-13	1340
liquid N <sub>2</sub>	77	8.90	807	0.162	1.1	298	3-5,7	539
acetone	329	18.2	727	0.242	1.6	523	5-10	601
methanol	338	18.9	748	0.295	1.6	523	6-10	511
ethanol	352	18.6	750	0.420	1.6	523	7-11	355
isopropanol	356	15.7	723	0.460	1.5	523	9,10	283

TABLE 1. Physical properties of different liquids at the boiling point  $T_b$  (K). Units are as follows:  $\gamma$  (mN/m),  $\rho_l$  (kg/m<sup>3</sup>),  $\eta_l$  (mPa s),  $l_c$  (mm). Data was taken from Lemmon *et al.* (2011). The last three columns indicate the range of substrate temperatures,  $T_s$  (K), used in the experiments, the observed mode numbers ( $n$ ), and the Reynolds number computed in §3.5.

one for ethanol, methanol, acetone, and isopropanol, and one for liquid N<sub>2</sub>, considering their respective capillary lengths ( $l_c$ ) listed in table 1. For some experiments, a plano-concave, fused silica lens (focal length = 250 mm) was used as the heated substrate in order to allow for optical imaging of the capillary waves underneath the Leidenfrost drop. A T-type thermocouple (maximum measurable temperature: 473 K, tip diameter  $\approx$  0.08 cm, HYP-2, Omega Engineering) was used to measure the internal temperature profile of Leidenfrost drops.

For most of the substrates, a pressure sensor (GEMS Sensors, response time: 5 ms, sensitivity: 2 mV/Pa) was connected to a hole (diameter = 1 mm) at the center of the curved substrate in order to measure the pressure variations in the vapor layer at sample rates of 500-1000 Hz during quiescent and oscillatory phases of drops as illustrated in figure 1(b). We used a high-speed digital camera (Phantom V7.11, Vision Research) with a resolution of about 132 pixels/cm to image the motions of drops from above at frame rates of 1000 frames per second. Recorded videos were then analyzed with NIH ImageJ software to obtain the frequency and wavelength of the star-shaped oscillations (A typical star-shaped oscillation mode  $n = 8$  is schematically shown in figure 1(c)).

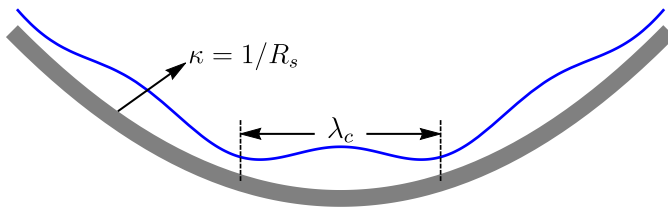


FIGURE 2. (Color online) Schematics of the suppression of Rayleigh-Taylor instability at the liquid interface (solid blue curve) by a curved substrate (solid gray curve) with a curvature  $\kappa = 1/R_s$ , where  $R_s$  is the radius of curvature defined before,  $\lambda_c$  is the capillary wavelength.

### 3. Results and discussions

#### 3.1. The geometry of Leidenfrost drops on curved surfaces

The shape of a Leidenfrost drop is determined by a competition between surface tension and gravity. It has been shown that a nonwetting drop with radius  $R \ll l_c$  will exhibit a quasi-spherical profile except for the bottom region where the drop is slightly flattened by gravity, which still holds true for small Leidenfrost drops (Burton *et al.* 2012). In comparison, for large Leidenfrost drops, i.e.  $R \gg l_c$ , the shape of the drops is dominated by gravity and resembles a circular puddle with a constant thickness of approximately  $2l_c$  (Biance *et al.* 2003). However, these large puddles are susceptible to the Rayleigh-Taylor instability, which is manifested by bubbles rising from the vapor layer beneath the drop (Biance *et al.* 2003). In our experiment, we used curved surfaces (see §2) in order to suppress the Rayleigh-Taylor instability and obtain large, stable Leidenfrost drops (Snoeijer *et al.* 2009; Quéré 2013; Trinh *et al.* 2014).

The effects of surface curvature on the Rayleigh-Taylor instability can be seen through the following simple model, similar to the original model used by Biance *et al.* (2003). Assuming the liquid-vapor interface beneath a Leidenfrost drop is perturbed with axisymmetric, sinusoidal variations, as illustrated in figure 2, then the new drop interface can be expressed in cylindrical coordinate as

$$S(r) = e + \frac{r^2}{2R_s} + \epsilon \cos\left(\frac{2\pi r}{\lambda_c}\right), \quad (3.1)$$

where  $e$  is the mean vapor layer thickness,  $\epsilon$  is the perturbation amplitude, and  $\lambda_c$  is the capillary wavelength generated at the bottom of the drop (see figure 11). We also assume that  $R_s \gg e \gg \epsilon$ , implying a small perturbation to the equilibrium shape of the drop (Duchemin *et al.* 2005; Lister *et al.* 2008). For a stable interface, the pressure at the drop center should be smaller or equal to the pressure at  $r \approx \lambda_c/2$  in order to drive liquid back to the center. If the pressure in the vapor layer is constant, then to leading order, the pressures at  $r = 0$ , and  $r = \lambda_c/2$  are

$$P_0 \approx \gamma\kappa|_{r \rightarrow 0} = 2\gamma \left( \frac{1}{R_s} - \frac{4\epsilon\pi^2}{\lambda_c^2} \right), \quad (3.2)$$

$$P_1 \approx \gamma\kappa|_{r \rightarrow \lambda_c/2} - \rho_l g \Delta z = \frac{4\epsilon\pi^2\gamma}{\lambda_c^2} + \frac{2\gamma + \rho_l g \lambda_c}{2R_s} - 2\epsilon\rho_l g, \quad (3.3)$$

where the height difference between the two points is  $\Delta z = S(r)_{r \rightarrow 0} - S(r)_{r \rightarrow \lambda_c/2} = 2\epsilon - \lambda_c^2/8R_s$ . The condition for stability can be found by equating (3.2) and (3.3), leading

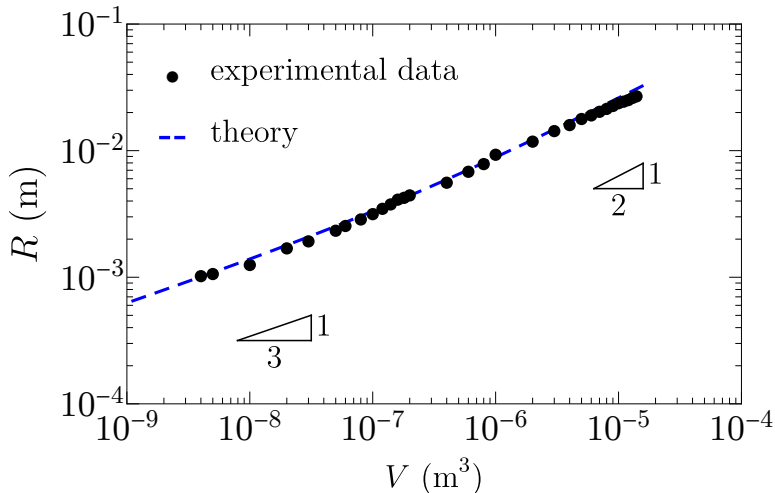


FIGURE 3. (Color online) The variations of drop radius  $R$  with respect to volume  $V$  for Leidenfrost water drops. The dashed blue line shows the theoretical prediction for a drop on a flat surface assuming that the contact angle of the drop is  $180^\circ$  as indicated in the text

to an expression for the wavelength:

$$\lambda_c = 2 \left( 2\epsilon R_s - \frac{\sqrt{2\rho_l g \epsilon R_s (-3\pi^2 \gamma + 2\rho_l g \epsilon R_s)}}{\rho_l g} \right)^{1/2}. \quad (3.4)$$

Since the perturbation amplitude and radius of curvature always appear as a product, (3.4) can also be written as

$$\frac{\lambda_c}{l_c} = 2 \left( 2\chi - \sqrt{2\chi(2\chi - 3\pi^2)} \right)^{1/2}, \quad (3.5)$$

where  $\chi = \epsilon R_s / l_c^2$ . For finite  $\epsilon$ , in the limit  $R_s \rightarrow \infty$ , (3.4) simplifies to  $\lambda_c / 2 \approx 3.85 l_c$ , in agreement with the prediction in [Biance \*et al.\* \(2003\)](#) for a flat surface. However, the addition of a curved surface couples the perturbation amplitude to the radius of curvature. The quantity  $2\chi - 3\pi^2$  must be positive in order for  $\lambda_c$  to be real, and thus represent the condition for instability. Subsequently, on a curved surface, the perturbation amplitude must satisfy  $\epsilon \gtrsim 14.8 l_c^2 / R_s$  in order to lead to the Rayleigh-Taylor instability.

Although the curved surface suppresses the Rayleigh-Taylor instability, it still has an affect on the overall drop shape. We investigated the influence of surface curvature on the drop shape by depositing water drops of given volumes  $V$  on a curved surface with  $T_s = 623$  K. We measured the radius  $R$  of the drops from recorded images taken immediately after deposition prior to the onset of oscillations. As can be seen in figure 3, stable Leidenfrost drops with  $R \approx 11 l_c$  are obtained on the curved surface, while on a flat substrate, the maximum radius of a stable Leidenfrost drop is  $R \approx 3.95 l_c$  ([Snoeijer \*et al.\* 2009](#); [Biance \*et al.\* 2003](#); [Burton \*et al.\* 2012](#)), suggesting that surface curvature plays a crucial role in suppressing the Rayleigh-Taylor instability. The dashed blue line in figure 3 shows the theoretical prediction for a drop on a flat surface by solving the Young-Laplace differential equation numerically and assuming that the contact angle of the drop is  $180^\circ$  ([Burton \*et al.\* 2010, 2012](#)). The experimental results show excellent agreement with the theoretical prediction, indicating that the shape of the Leidenfrost drops is not strongly affected by the surface curvature. More specifically, when  $R < l_c$  (2.5 mm), the drops are

quasi-spherical and thus  $R \propto V^{1/3}$ , whereas  $R \propto V^{1/2}$  for  $R > l_c$ , which is expected for puddle-like drops with constant thickness.

However, one can also notice that most of the experimental data is slightly less than the corresponding theoretical prediction, which we attribute to two possible reasons. First, for small drops, the evaporation begins from the moment of deposition on the hot surface, which removes a small amount of water prior to imaging. Second, large drops are thicker in the center due to the underlying curved substrate, leading to a smaller apparent radius for a given volume. Thus, although surface curvature and evaporation may somewhat reduce the drop size, the effects seem to be a minor influence on the overall drop shape.

### 3.2. “Breathing mode” of small Leidenfrost drops

Caswell (2014) experimentally characterized axisymmetric oscillations in the radius of small Leidenfrost drops using interference imaging. The drops displayed small-amplitude changes in the radius of the flat region near the surface. Due to volume conservation, an increase (decrease) in the drop radius leads to a decrease (increase) in the thickness of the drop. Caswell (2014) found that the oscillation frequency of the breathing mode,  $f_b$ , obeyed a distinct power law,  $f_b \propto R_0^{-0.68 \pm 0.01}$ , where  $R_0$  is the average drop radius during the oscillation. This dependence is distinctly different than the expected three-dimensional dispersion relation for inviscid spherical drops,  $f \propto R_0^{-3/2}$  (Rayleigh 1879). Here we provide an analytical model which explains this contrast and fits the experimental data with no adjustable parameters.

To leading order, and due to the axisymmetry of the breathing mode, we model a Leidenfrost drop as an incompressible liquid cylinder of volume  $= V$  and a time dependent radius,  $R(t)$ . We will assume that the bottom of the cylinder is fixed at  $z = 0$ , which is reasonable if the thickness of the vapor layer varies much less than the radius. In cylindrical coordinates,  $(r, \phi, z)$ , the simplest form for the velocity which satisfies  $\nabla \cdot \vec{v} = 0$  and the boundary conditions  $\vec{v} \cdot \hat{r}|_{r=R(t)} = R'(t)$  and  $\vec{v} \cdot \hat{z}|_{z=0} = 0$  is:

$$\vec{v} = \frac{R'(t)}{R(t)} (r, 0, -2z). \quad (3.6)$$

For simplicity, we will write  $R(t) = R$ , and  $R'(t) = R'$ . The total kinetic energy of the drop is then:

$$T = \int \frac{1}{2} \rho_l |\vec{v}|^2 dV = \frac{\pi \rho_l R^2}{R'^2} \int_0^R \int_0^h r (r^2 + 4z^2) dz dr. \quad (3.7)$$

Evaluating the integrals, and using the fact that  $V = \pi R^2 h$ , where  $h$  is the time-dependent height of the cylinder, we obtain

$$T = \frac{1}{12} \rho_l V \left( 3 + \frac{8V^2}{\pi^2 R^6} \right) R'^2. \quad (3.8)$$

The total potential energy is the sum of gravitational potential energy and surface energy:

$$U = \frac{1}{2} \rho_l V g h + 2\pi \gamma R (h + R) = \frac{gV^2 \rho_l + 4\pi \gamma R (V + \pi R^3)}{2\pi R^2}. \quad (3.9)$$

The equilibrium drop radius,  $R_0$ , can be found by minimizing the potential energy with respect to  $R$ ,

$$\frac{dU}{dR} = 0 = 4\pi \gamma R_0 - \frac{2V\gamma}{R_0^2} - \frac{g\rho_l V^2}{\pi R_0^3}. \quad (3.10)$$

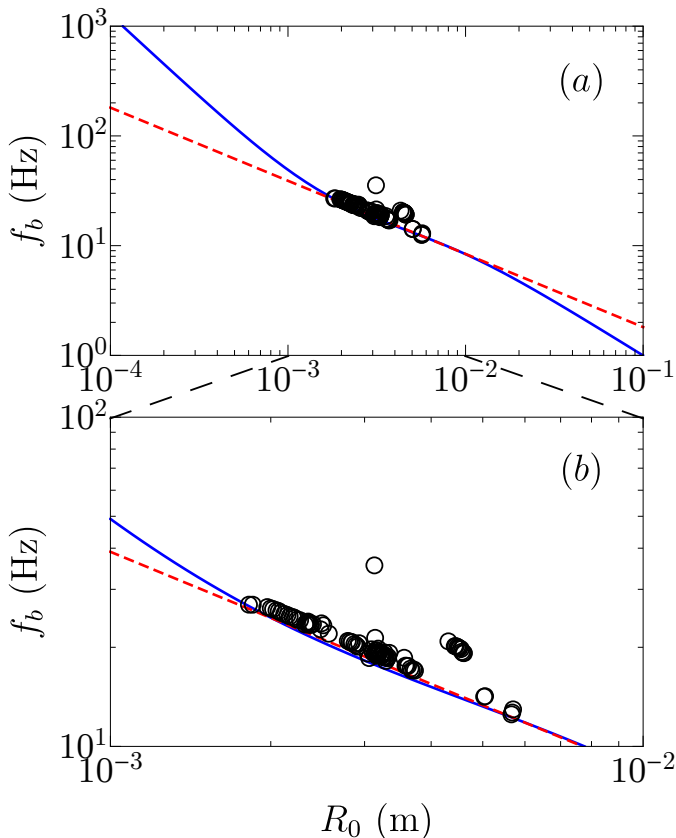


FIGURE 4. (Color online)(a) Breathing mode oscillation frequency  $f_b$  of small Leidenfrost drops as a function of the average drop radius  $R_0$ . The dashed red curve represents the power law  $f_b \propto R_0^{-0.68}$ , and the solid blue curve represents the dispersion relation from (3.13). (b) A zoomed-in view of the data in (a). With permission, the data shown here is taken from Caswell (2014).

For large drops where  $R \gg h$ , the first and third terms must balance. Equating these two terms and using the fact that  $V = \pi R^2 h$ , we see that

$$h \approx 2\sqrt{\frac{\gamma}{\rho_l g}}, \quad R_0 \rightarrow \infty, \quad (3.11)$$

which agrees with the expected asymptotic thickness of large Leidenfrost drops (Biance *et al.* 2003). We may now define the Lagrangian of the system as  $L = T - U$ , and apply the Euler-Lagrange equation to obtain a differential equation for  $R$ :

$$R'' = \frac{6\rho_l V^2 g \pi R^4 + 12\gamma V \pi^2 R^5 - 24\gamma \pi^3 R^8 + 24\rho_l V^3 R^2}{8\rho_l V^3 R + 3\rho_l V \pi^2 R^7}. \quad (3.12)$$

To proceed further, we will linearize the equation by considering only small oscillations of the radius,  $R = R_0(1 + \epsilon e^{i\omega t})$ , where  $R_0$  is equilibrium drop radius found by solving (3.10),  $\epsilon$  is the perturbation amplitude, and  $\omega$  is the angular frequency of the oscillation. Assuming that  $\epsilon \ll 1$ , to leading order (3.12) reduces to an expression for the angular



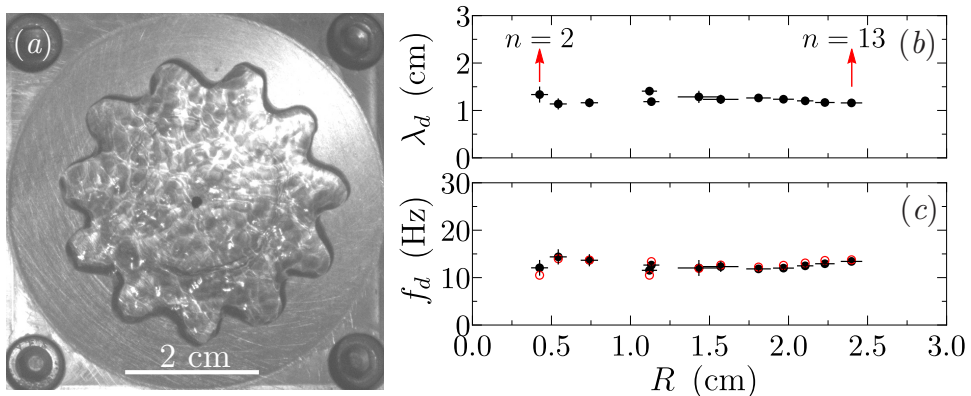


FIGURE 5. (Color online) Star-shaped oscillations of Leidenfrost water drops at  $T_s = 623$  K. (a) A snapshot of the oscillation mode with  $n = 11$ . (b) and (c) show the star-shaped oscillation wavelength  $\lambda_d$ , and frequency  $f_d$ , with respect to drop radius  $R$ . The data points from left to right in (b) and (c) represent the increasing mode number  $n$  as indicated by the red arrows, and the error bars in (b) and (c) are the standard deviations of multiple drops. The data for  $\lambda_d$  in (b) are indirectly measured using the relation  $2\pi R = n\lambda_d$ , and the red circles in (c) represent the theoretical prediction by (3.16) for drops with different radii.

frequency:

$$\omega^2 = \frac{576\gamma^2(\gamma + \Gamma) + 36\rho_l^2 g^2 R_0^4(\gamma + 2\Gamma) + 384\gamma\rho_l g R_0^2(5\gamma + 2\Gamma)}{\rho_l R_0^3(1120\gamma^2 + 9\rho_l^2 g^2 R_0^4 + 192\gamma\rho_l g R_0^2)}, \quad (3.13)$$

where  $\Gamma \equiv \sqrt{\gamma^2 + 4\gamma\rho_l g R_0^2}$  and we have substituted  $V$  for the equilibrium radius  $R_0$  using (3.10).

Taking typical values of the parameters in (3.13) for water, we can plot the oscillation frequency of the breathing mode,  $f_b = \omega/2\pi$ , as a function of  $R_0$ , which is shown by the solid blue curve in figure 4(a). The theory shows excellent agreement with the data. For comparison, the power law  $f_b \propto R_0^{-0.68}$  found by Caswell (2014) is plotted as the dashed red line in figure 4(a). A closer view of the comparison between the prediction by (3.13) and  $f_b \propto R_0^{-0.68}$  can be seen in figure 4(b). The data lie in the transition regime between two asymptotic limits,  $R_0 \ll l_c$  and  $R_0 \gg l_c$ , which may explain the anomalous power law reported by Caswell (2014). In these two limits, (3.13) reduces to

$$\begin{aligned} \omega &\approx \left( \frac{36\gamma}{35\rho_l R_0^3} \right)^{1/2}, & R_0 \rightarrow 0 \\ \omega &\approx \frac{4}{R_0} \left( \frac{g\gamma}{\rho_l} \right)^{1/4}, & R_0 \rightarrow \infty. \end{aligned} \quad (3.14)$$

The scaling for small drops is independent of  $g$ , which is expected based on their nearly-spherical shape. For large drops where  $h \approx 2l_c$  (3.11), the scaling is determined essentially by gravity:  $\omega \sim \sqrt{2gh}/R_0$ .

### 3.3. Star-shaped oscillations of Leidenfrost water drops

In addition to the breathing mode, large Leidenfrost drops may also develop azimuthal, star-shaped oscillations. Similar oscillations have been observed in a variety of systems involving liquid drops (Brunet & Snoeijer 2011). In our experiments with Leidenfrost water drops using a curved substrate, we observe star-shaped oscillation modes with  $n = 2$  to 13 lobes along the drop periphery at  $T_s = 623$  K. A typical star-shaped oscillation

mode ( $n = 11$ ) is shown in figure 5(a). Figures 5(b) and 5(c) show the drop oscillation wavelength  $\lambda_d$  and frequency  $f_d$  for different  $R$ , respectively, which are measured by analyzing the high-speed videos of the oscillating drops. Surprisingly, both  $\lambda_d$  and  $f_d$  remained nearly constant as we varied  $R$ . Increasing  $R$  thus led to an increase in the allowable number of lobes  $n$ , as indicated by the red arrows. This similar trend also applies to other liquids used in our experiments, which will be discussed in §3.5.

For the free oscillations of an incompressible, axisymmetric spherical drop with infinitesimal deformations, the natural resonance frequency,  $f_n$ , of the  $n$ th-mode is given by (Rayleigh 1879):

$$f_n = \frac{1}{2\pi} \sqrt{\frac{n(n-1)(n+2)}{\rho_l R^3}}. \quad (3.15)$$

For a liquid puddle with  $R \gg h \approx 2l_c$ , where  $h$  is the thickness of the liquid puddle (Biance *et al.* 2003), the resonance frequency  $f_n$  takes the form (Yoshiyasu *et al.* 1996):

$$f_n = \frac{1}{2\pi} \sqrt{\frac{n(n^2-1)}{\rho_l R^3}} \sqrt{\frac{1}{1 + (2 - \frac{\pi}{2} + \frac{n-3}{4}) \frac{l_c}{R}}}. \quad (3.16)$$

The first term under the square root is for a strictly two-dimensional drop, whereas the correction factor,  $1/\sqrt{1 + (2 - \frac{\pi}{2} + \frac{n-3}{4}) \frac{l_c}{R}}$ , is due to the quasi-two-dimensional nature of the puddle.

As shown in figure 5, for water drops where we observed  $n = 2$  modes, the average radius was  $R \approx 4$  mm, which is greater than  $l_c$ . Hence, it is reasonable to use (3.16) to predict the oscillation frequency for all star-shaped modes in our experiments. The comparison between theory and experiment is shown in figure 5(c), which indicates an excellent agreement. For smaller values of  $n$ , both  $\lambda_d$  and  $f_d$  vary non-monotonically with  $R$ . There are a few potential reasons for this. One possibility is that nonlinear effects play a more significant role for smaller values of  $n$  because the ratio of the mode amplitude to the drop radius is larger (Becker *et al.* 1991; Smith 2010). However, the excellent agreement with the linear theory, i.e. (3.16), suggests that nonlinear effects may not be important.

Instead, we suggest that the behavior may be related to the mode selection mechanism. For a given radius, either the frequency or the wavelength is preferentially selected by the excitation mechanism. Once  $f_d$  or  $\lambda_d$  is selected, (3.16) will determine the other. As will be shown in §3.6, there are strong capillary waves excited at the liquid-vapor interface beneath the drop. These waves produce pressure oscillations which parametrically couple to the star-shaped modes. A determination of the expected behavior of  $f_d$  on  $R$  is thus complicated by the physics of the vapor flow beneath the drop, nevertheless, we would expect the effects to be less variable for  $R \gg \lambda_d$ , which agrees with the data shown in figure 5.

### 3.4. Pressure oscillations in the vapor layer

It has been well-documented that star oscillations of large liquid drops can be initiated by a parametric forcing mechanism (Brunet & Snoeijer 2011). For instance, when a liquid puddle is deposited onto a superhydrophobic, vertically-vibrating substrate with a prescribed frequency, then the equation of motion of the drop can be described by an equation similar to Mathieu's equation, and star oscillations will be excited when the drop oscillation frequency is approximately half that the excitation frequency (Yoshiyasu *et al.* 1996; Brunet & Snoeijer 2011). In the experiment, we observed star oscillations

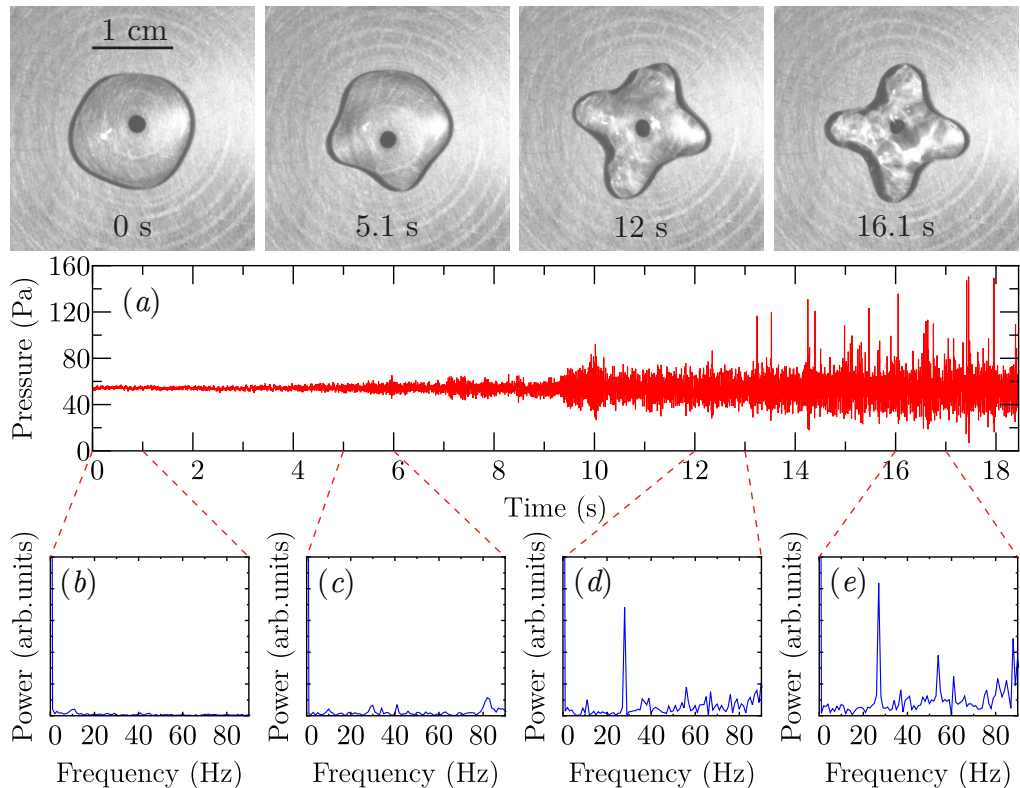


FIGURE 6. (Color online) (a) The pressure variations in the vapor layer during the initiation of a 4-mode star-shaped oscillation of a Leidenfrost water drop within  $\approx 18.5$  s. (b), (c), (d), and (e) represent the Fourier power spectra of the pressure in the vapor layer during the time intervals of 0-1 s, 5-6 s, 12-13 s, and 16-17 s, respectively. The snapshots of the top panel represent the drop profile at 0 s, 5.1 s, 12 s, and 16.1 s, respectively, during the initiation process.

of Leidenfrost water drops (e.g. see figure 5a) in the absence of an external excitation. Therefore, we hypothesize that the star oscillations are driven by fluctuations in the vapor layer pressure that supports the drop.

In order to explore the dynamics of pressure fluctuations in the vapor layer, we utilized a pressure sensor attached to the center of the curved substrate, schematically shown in figure 1(b). We measured the pressure variations in the vapor layer of water drops at  $T_s = 623$  K during the initiation of the star-shaped oscillations. We started recording the pressure immediately after the drops were placed on the substrate, and stopped after the well-defined star-shaped oscillations had been initiated for several seconds. The whole process lasted about 18.5 s.

The snapshots on the top panel of figure 6(a) show images of an  $n = 4$  drop at different stages during the oscillation. More specifically, the drop shape was nearly circular immediately upon placement on the substrate ( $t = 0$  s), then the pressure fluctuations in the vapor layer increased as the drop shape developed well-defined lobes. The amplitude continued to grow with time ( $t = 12$  s) until the formation of a steady-state, star-shaped oscillation with large amplitude ( $t = 16.1$  s).

Figure 6(a) shows the pressure variations in the vapor layer during the whole process. The mean pressure required to support the drop is  $\rho_l g h \approx 2\rho_l g l_c = 47$  Pa. However, the mean pressure we measure is slightly larger than this value because the pressure is

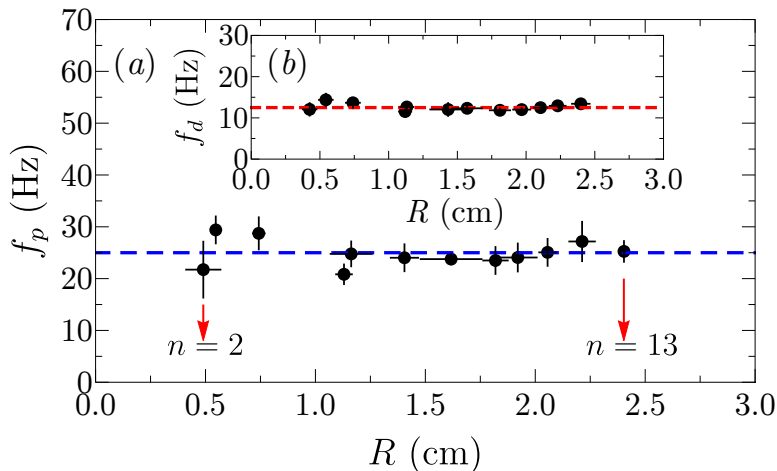


FIGURE 7. (Color online) (a) Summary of the pressure oscillation frequencies  $f_p$  in the vapor layer of star-shaped Leidenfrost water drops with different radii at  $T_s = 623$  K. The data points from left to right represent the oscillation modes from  $n = 2$  to 13, respectively, as indicated by the red arrows. (b) The drop oscillation frequency  $f_d$  with respect to drop radius  $R$  (figure 5c). The error bars of  $f_p$  are taken from the full-width at half-max of the highest peak in the Fourier power spectra computed over a time interval of 10 s, and the error bars of  $R$  are defined as the standard deviation of multiple measurements of different drops after the star oscillations are fully developed for each mode. The dashed lines in (a) and (b) are visual guides to indicate that  $f_p \approx 2f_d$ .

measured at the center of the substrate where the the pressure is larger in order to drive the viscous vapor to flow out to the drop edge. The pressure fluctuations around the mean increase with time until the formation of a steady star-shaped oscillation with a large amplitude (about  $t = 14$  s).

In order to gain insight into the underlying relationship between the oscillations of the drop and pressure in the vapor layer, we performed a Fast Fourier Transform on the pressure data in four different time intervals: 0-1 s, 5-6 s, 12-13 s, and 16-17 s. The results are shown in figures 6(b)-6(e). Initially, the pressure remains nearly constant, and there are no sharp peaks in the power spectrum (figure 6b). Between  $t = 5-6$  s, the pressure fluctuations become stronger and more periodic, and several small peaks are visible (figure 6c). Then, as the star oscillation is further developed, a sharp peak which is located at  $\approx 28$  Hz shows up in the power spectrum (figure 6d). Finally, when the star oscillation is fully developed, the pressure fluctuations stop growing, and a sharp peak located at  $\approx 28$  Hz dominates the spectrum (figure 6e).

It is interesting to note that the location of the sharp peak is approximately twice the oscillation frequency of a fully-developed,  $n = 4$  mode Leidenfrost water drop (see figure 5c). This is consistent with a parametric forcing mechanism for the excitation of the star oscillations. Moreover, harmonics at higher frequencies are also visible as indicated by the secondary peaks in figure 6(e). This is likely due to nonlinear effects involved in the star-shaped oscillations. In addition, the location of the peak is robust. As will be shown in §3.7, the location of the dominant peak in the power spectrum is mostly independent of the substrate temperature and the environmental temperature.

Figure 7(a) shows the pressure oscillation frequency  $f_p$  in the vapor layer of Leidenfrost water drops for all of the observed modes. The data points from left to right correspond the oscillation modes from  $n = 2$  to 13, as indicated by the red arrows. By comparing this with the drop oscillation frequency  $f_d$  (figure 7b), we find  $f_p \approx 2f_d$  as indicated by the

dashed blue and red lines in figures 7(a) and 7(b), respectively. This robust relationship suggests that the star-shaped oscillations are parametrically driven by the pressure (Miles & Henderson 1990; Kumar & Tuckerman 1994; Yoshiyasu *et al.* 1996; Brunet & Snoeijer 2011; Terwagne & Bush 2011). Consider the radial position of a point on the perimeter of the drop during a star-shaped oscillation,  $r(t)$ . This point will oscillate in time due to the azimuthal standing wave, and obey the following equation:

$$\frac{d^2r}{dt^2} + \omega^2 r = 0. \quad (3.17)$$

To leading order,  $\omega$  is the resonant frequency of the mode, (3.16):

$$\omega_0^2 = \frac{n(n^2 - 1)\gamma}{\rho_l R^3}. \quad (3.18)$$

For simplicity, we have ignored the correction due to the quasi-two-dimensional nature of the drop. The pressure variations will induce vertical oscillations of the drop, and in turn oscillations of the drop radius:

$$R = R_0(1 + \epsilon \cos \omega_p t), \quad (3.19)$$

where  $R_0$  is the average radius of the drop, and  $\epsilon$  is the amplitude of the small perturbation. Plugging (3.19) into (3.18), to leading order in  $\epsilon$  we obtain  $\omega^2 = \omega_0^2(1 - 3\epsilon \cos \omega_p t)$ . Therefore, (3.17) now becomes:

$$\frac{d^2r}{dt^2} + \omega_0^2(1 - 3\epsilon \cos \omega_p t)r = 0. \quad (3.20)$$

When  $\omega_p \approx 2\omega_0$ , the parametric resonance is the strongest, i.e. the oscillation amplitude will exponentially increase with time until the star-shaped oscillations are fully developed. This is consistent with our measurements of the pressure oscillation frequencies in the vapor layer (figure 7), which are approximately twice that the drop oscillation frequencies (figure 5c) that we observed in our experiment. We note that it is possible that the pressure oscillations are a *consequence* of the star oscillations. If the star oscillations were excited by some other mechanism, then the symmetry of the star shape would necessitate a pressure extrema when the star shape reaches its maximum amplitude. However, the only energy which is available to drive the oscillation comes from the evaporation and gas flow in the vapor layer. Thus we expect that the pressure oscillations are the source of the star oscillations. §3.6 will explore the potential source of the pressure oscillations.

### 3.5. Star-shaped oscillations of different liquids

In addition to water, we performed similar experiments with five other liquids: liquid N<sub>2</sub>, acetone, methanol, ethanol, and isopropanol. For these liquids, the curved surfaces were also machined to satisfy  $l_c/R_s \approx 0.03$  (see §2), and the relevant physical properties and substrate temperatures are listed in table 1. Figure 8 shows snapshots of star-shaped oscillations for the six different liquids we used in the experiments, where the other five liquids show similar star-shaped patterns to water drops but with different observable oscillation modes. By analyzing the images of the star-shaped oscillations, we find that star-shaped oscillations of acetone, methanol, ethanol, and isopropanol share a similar wavelength  $\lambda_d \approx 0.9$  cm and frequency  $f_d \approx 14$  Hz, whereas liquid N<sub>2</sub> shows a wavelength of  $\lambda_d \approx 0.6$  cm and frequency  $f_d \approx 17$  Hz. This suggests that the star oscillations may depend on the capillary length of the liquid.

Figure 9 shows the dependence of star-shaped oscillation mode  $n$ , rescaled wavelength  $\lambda_d/l_c$ , and rescaled frequency  $f/\sqrt{g/l_c}$  on the rescaled drop radius  $R/l_c$  of the six liquids

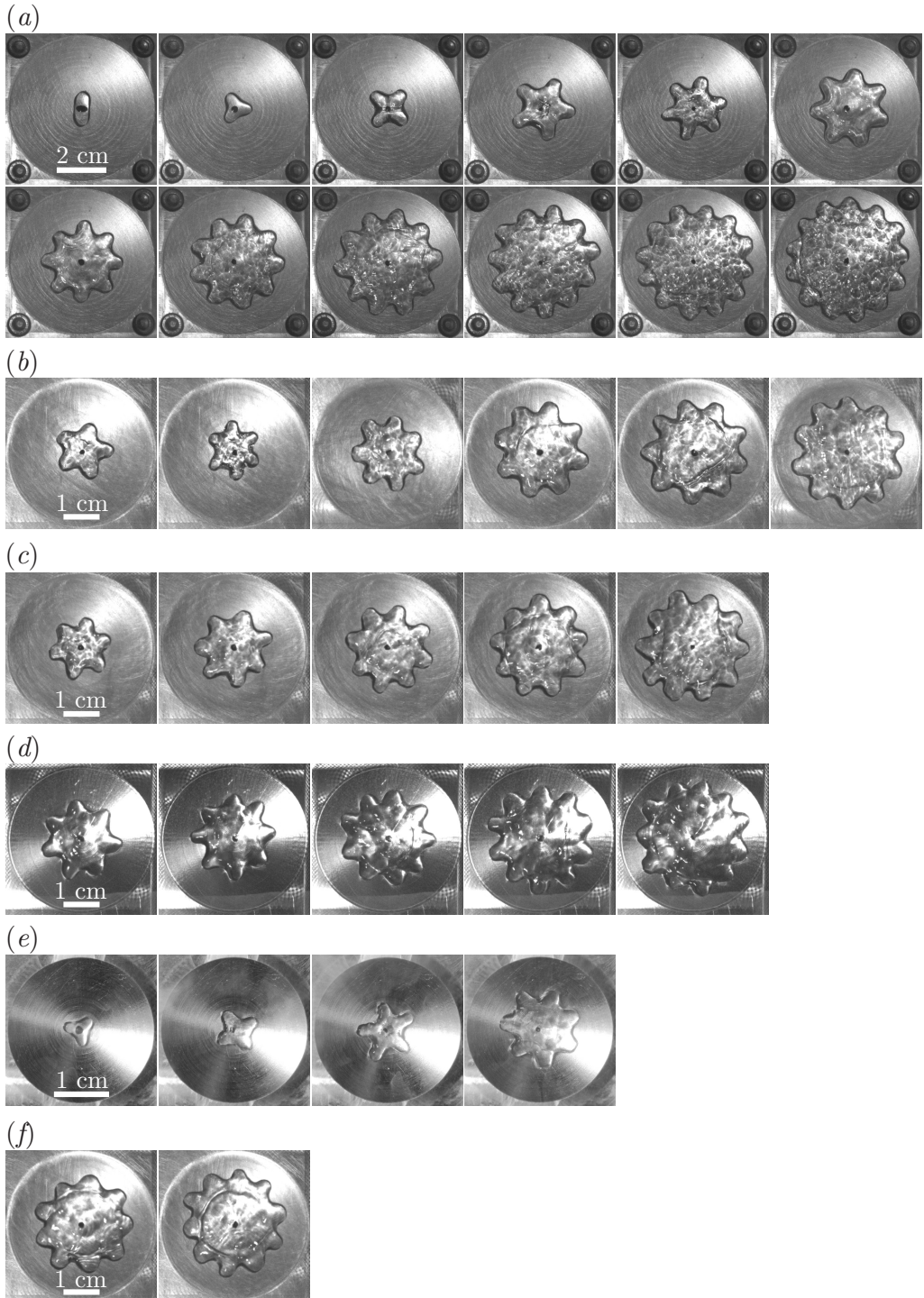


FIGURE 8. (Color online) Snapshots of star-shaped oscillation modes with  $n = 2$  to 13 of six different liquids when the lobes are at their maximum displacement. Panels (a), (b), (c), (d), (e), and (f) represent water, acetone, methanol, ethanol, liquid  $N_2$ , and isopropanol, respectively. For water:  $T_s = 623$  K, for acetone, methanol, ethanol and isopropanol:  $T_s = 523$  K. The substrate for liquid  $N_2$  was not heated.

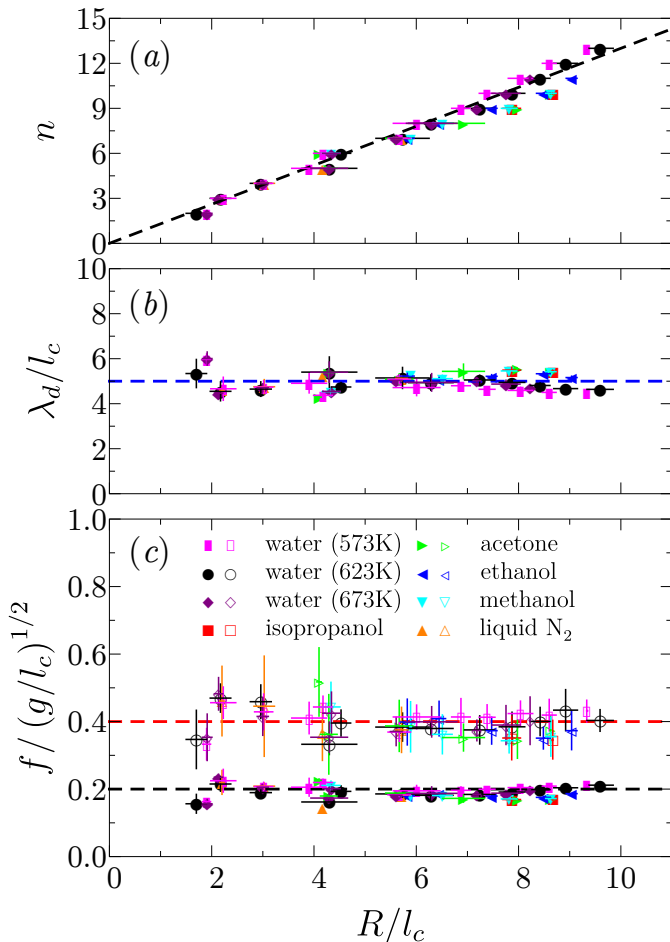


FIGURE 9. (Color online) Dependence of star-shaped oscillation mode  $n$  (a), and dimensionless oscillation wavelength  $\lambda_d/l_c$  (b) and frequency  $f/\sqrt{g/l_c}$  (c) with respect to the dimensionless drop radius  $R/l_c$  for six different liquid. In (c), the solid symbols represent the drop oscillation frequency  $f_d$ , whereas the open symbols denote the corresponding pressure oscillation frequency  $f_p$ . The error bars of  $R$ ,  $\lambda_d$  and  $f_d$  come from the standard deviations of multiple measurements of different drops, and the error bars of  $f_p$  are defined as the full width of the highest peak in the power spectrum at half the maximum value. The dashed lines in all panels are visual guides.

used in the experiment. The mode number  $n$  increases linearly with  $R/l_c$  as indicated by the dashed black line in figure 9(a), showing that large modes can only be observed in larger drops, as supported by figure 8. The rescaled wavelength  $\lambda_d/l_c$  for the six liquids collapses onto a straight line as shown in figure 9(b), which indicates that the wavelength of the star oscillations only depends on  $l_c$  of the liquid. Figure 9(c) shows the oscillation frequency of both the azimuthal star oscillations,  $f_d$ , and the corresponding pressure,  $f_p$ , in the vapor layer. The solid symbols denote the drop oscillations, whereas open symbols with the same color represent the corresponding pressure oscillations in the vapor layer for a specific liquid. Both  $f_d$  and  $f_p$  collapse fairly well, and the relationship  $f_p \approx 2f_d$  is consistent with the data, as indicated by the dashed black and red lines. Additionally, by comparing different values of  $T_s$  for water, figure 9 shows that  $\lambda_d$ ,  $f_d$ , and  $f_p$  are mostly independent of substrate temperature.

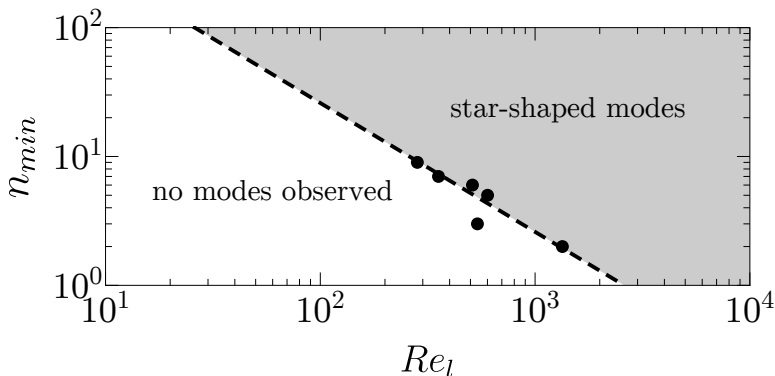


FIGURE 10. Scaling behavior for the minimum observed star mode  $n_{min}$  with respect to  $Re_l$  of different liquids (table 1). The dashed line represents the fit to the data,  $2600 Re_l^{-1}$ .

The main influence of  $T_s$  is through the number of observable modes. For instance, at  $T_s = 673$  K, we did not observe oscillation modes  $n = 12$  and  $n = 13$  in water, which we attribute to the extremely fast evaporation rate of the liquid, as will be discussed in §3.6. Although the robust relationship between  $f_d$  and  $f_p$  suggests that the star oscillations of the drops are parametrically driven by the pressure in the vapor layer, there is an interesting variation in both  $f_d$  and  $f_p$  at small mode numbers. The data for smaller modes (e.g.  $n = 2, 3, 4$ ) deviates further from the average compared to larger modes. This behavior may be nonlinear in nature since the amplitude of the mode relative to the drop radius is much larger for small  $n$  (Becker *et al.* 1991; Smith 2010). In addition, the quasi-two-dimensional nature of the drop is more important at small  $n$ , which may also contribute to the variations in this regime. A more quantitative explanation for this dependence is left for future studies.

As shown in table 1, different oscillation modes are observed in different liquids. In particular, some liquids failed to display smaller mode numbers. This may be due to inherent viscous damping that prevents the sustained excitation of large-amplitude oscillations. Following the analysis in Ma *et al.* (2017), the role of damping can be characterized by the Reynolds number associated with the liquid oscillation. For a star oscillation, the characteristic length scale and time scale are  $l_c$  and  $\sqrt{l_c^3 \rho_l / \gamma}$ , respectively. Thus, the inertial term in the Navier-Stokes equation is estimated as  $|\rho_l(\vec{v} \cdot \nabla)\vec{v}| = \gamma / l_c^2$ , and the viscous term is  $|\eta_l \nabla^2 \vec{v}| = \eta_l / \sqrt{l_c^5 \rho_l / \gamma}$ . The Reynolds number of the oscillating liquid is defined as the ratio of inertial to viscous terms:  $Re_l = \sqrt{l_c \rho_l \gamma} / \eta_l$ , and the values of  $Re_l$  for different liquids are listed in table 1.

Figure 10 shows the dependence of the minimum mode number  $n_{min}$  on  $Re_l$  for each liquid. The dashed line represents a suggested scaling  $Re^{-1}$ , indicating that the liquid viscosity damps the oscillations of smaller drops and thus sets the minimum mode number of stable star oscillations. However, the substrate temperature and thus evaporation rate will likely affect the number of observed modes as well. A higher evaporation rate will induce a stronger driving of the oscillation modes, which would reduce  $n_{min}$ . This can be seen in figure 10 for liquid  $N_2$ , which undergoes much more rapid evaporation due to the large difference between the boiling and substrate temperature,  $T_s - T_b$ . In addition, as mentioned previously, the stronger evaporation may also inhibit larger modes if the pressure oscillations are less coherent. In the next section we show how the flow in the vapor layer is linked to the pressure oscillations.



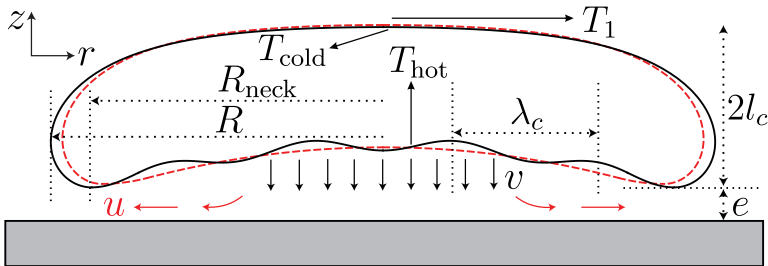


FIGURE 11. (Color online) Sketch of the cross-sectional view of a large Leidenfrost drop levitating on a flat hot surface. The red dashed line and black solid line represent the drop profiles before and after the initiation of capillary waves at the bottom surface of the drop. The symbols are defined in the main text.

### 3.6. Origin of pressure oscillations in the vapor layer

As evidenced by figure 9(c), the star-shaped oscillations of Leidenfrost drops are parametrically driven by the pressure variations in the vapor layer. Star oscillations induced by a parametric coupling have been observed in a variety of systems where variations of the drop radius are induced by external, periodically-modulated fields (Brunet & Snoeijer 2011). However, in our experiment, there are no obvious external fields. It is then crucial to understand the source of the pressure oscillations. In this section we show how capillary waves of a characteristic wavelength at the liquid-vapor interface induce the pressure oscillations in the vapor layer.

Figure 11 shows a sketch of a large, axisymmetric Leidenfrost drop with a maximum radius  $= R$  and thickness  $\approx 2l_c$ . The mean vertical velocity of the gas at the liquid surface is  $v$ ,  $e$  is the mean thickness of the vapor layer, and  $u$  is the outward radial velocity of the gas near  $r = R$ . For such a large Leidenfrost drop, both the bottom surface of the drop and the substrate surface are assumed to be approximately flat to simplify the analysis. Following the model of Bianco *et al.* (2003), the mass loss rate of the drop due to evaporation can be expressed as:

$$\frac{dm}{dt} = \frac{\kappa_v}{L} \frac{\Delta T}{e} \pi R^2 = \rho_v \pi R^2 v, \quad (3.21)$$

where  $\kappa_v$  is the thermal conductivity of the vapor,  $L$  is the latent heat of the evaporation,  $\Delta T = T_s - T_b$ , and  $\rho_v$  is the density of the vapor at the liquid interface. Since  $e \approx 100 \mu\text{m}$ , and thus  $R \gg e$  (Burton *et al.* 2012), we employ lubrication theory, leading to an expression relating the flow rate to the mean pressure,  $P$ , in the vapor layer:

$$\frac{dm}{dt} = \rho_v \frac{2\pi e^3}{3\eta_v} P = \rho_v \frac{2\pi e^3}{3\eta_v} 2l_c \rho_l g = \rho_v \pi R^2 v, \quad (3.22)$$

where  $\eta_v$  is the dynamic viscosity of the vapor. We note here that parameters such as  $\kappa_v$ ,  $\rho_v$ , and  $\eta_v$  will vary in the vapor layer due to the temperature gradient between the liquid and solid surfaces. For simplicity, we will assume that these represent average values of the vapor layer properties. A more detailed treatment, possibly including full numerical simulations, would be necessary to extend this simplified model.

In addition, due to mass conservation, the volumetric flow rate of gas from the bottom of the drop must be equal to the flow rate exiting the perimeter of drop:

$$\pi R^2 v = 2\pi e R u. \quad (3.23)$$

Solving (3.21), (3.22), and (3.23) for  $u$ ,  $v$ , and  $e$  yields:

$$u = \left( \frac{\rho_l g \kappa_v l_c}{3 \rho_v \eta_v L} \right)^{1/2} \Delta T^{1/2}, \quad (3.24)$$

$$v = \left[ \frac{4 l_c \rho_l g}{3 \eta_v} \left( \frac{\kappa_v \Delta T}{L \rho_v} \right)^3 \right]^{1/4} R^{-1/2}, \quad (3.25)$$

$$e = \left( \frac{3 \kappa_v \Delta T \eta_v}{4 L l_c \rho_l \rho_v g} \right)^{1/4} R^{1/2}. \quad (3.26)$$

In this model, the steady-state, linear temperature profile in the vapor layer is valid since the characteristic time scale associated with thermal diffusion,  $e^2/D_v \approx 1$  ms, is smaller than the typical residence time of the gas in the vapor layer,  $R/u \approx 10$  ms, where  $D_v$  is the thermal diffusivity of the vapor. Let us assume a water Leidenfrost drop with  $R = 0.01$  m, and for the vapor, we use the properties of steam at 373 K and 1 atm of pressure:  $\rho_l = 959$  kg/m<sup>3</sup>,  $\rho_v = 0.45$  kg/m<sup>3</sup>,  $\gamma = 0.059$  N/m,  $g = 9.8$  m/s<sup>2</sup>,  $L = 2.26 \times 10^6$  J/kg,  $\eta_v = 1.82 \times 10^{-5}$  Pa s, and  $\kappa_v = 0.04$  W/m/K. Although the properties of the vapor may vary somewhat in the vapor layer due to the temperature gradient, we have verified that this does not significantly affect our analysis.

We can now plot  $u$ ,  $v$ , and  $e$  with respect to  $\Delta T$  based on (3.24), (3.25) and (3.26). The results are shown in figures 12(a), 12(b), and 12(c), respectively. The inertial term in the Navier-Stokes equation is estimated as  $|\rho_v(\vec{v} \cdot \nabla)\vec{v}| = \rho_v v^2/e$ , and the viscous term as  $|\eta_v \nabla^2 \vec{v}| = \eta_v v/e^2$ . Thus the Reynolds number in the vapor layer is  $Re_v = \rho_v v e / \eta_v$ . Plugging in (3.25) and (3.26), we arrive at a surprisingly simple expression for the Reynolds number in the vapor:  $Re_v = \Delta T \kappa_v / L \eta_v$ , which is independent of the drop size. This expression is plotted in figure 12(d). Under typical experimental conditions,  $Re_v \approx 0.2$ , suggesting that the original lubrication flow assumption is valid, although inertial forces are non-negligible.

Based on figure 12, we can estimate the Bernoulli pressure in the vapor layer of Leidenfrost water drops as  $\rho_v u^2/2 \approx 1$  Pa, which is much smaller than the pressure variations  $\approx 10$  Pa (see figure 6a), suggesting that the inertial force does not account for the pressure variations. The viscous pressure is  $P_{\text{vis}} \sim \eta_v v R^2 / e^3$ , thus the pressure variation due to the local variations of the film thickness is  $\Delta P_{\text{vis}} = \frac{dP_{\text{vis}}}{de} \Delta e$ . Then  $\Delta P_{\text{vis}} = 10$  Pa corresponds to  $\Delta e \approx 15$   $\mu\text{m}$  considering the typical values of  $v$  (figure 12c) and  $R$ . Although this local film thickness could also be possibly induced by the vertical motion of the center of mass of the drops, the fact that small and large drops (see figure 9c) share a nearly constant oscillation frequency suggests this is not the case. Therefore, the pressure variations in the vapor layer are likely to be induced by the local variations of the vapor film thickness.

We propose that capillary waves with a characteristic wavelength,  $\lambda_c$ , traveling from the center to the edge of the drop lead to local variations in vapor film thickness, and thus pressure variations in the vapor layer, as schematically shown in figure 11. To confirm this possibility, we used a heated, plano-concave, fused silica lens as a substrate to image the capillary waves from below. The results for acetone and ethanol Leidenfrost drops are shown in figure 13. The images were produced by averaging all frames in a given video sequence, then subtracting this background image in order to enhance contrast in the center of the drop. The white ‘‘halo’’ surrounding the drop is a consequence of this subtraction process. The Fourier spectra for the capillary waves in the central region of the drops were computed in both time and space using the pixel intensity as the signal. Using the Nyquist sampling theorem, the maximum frequency was limited by half the

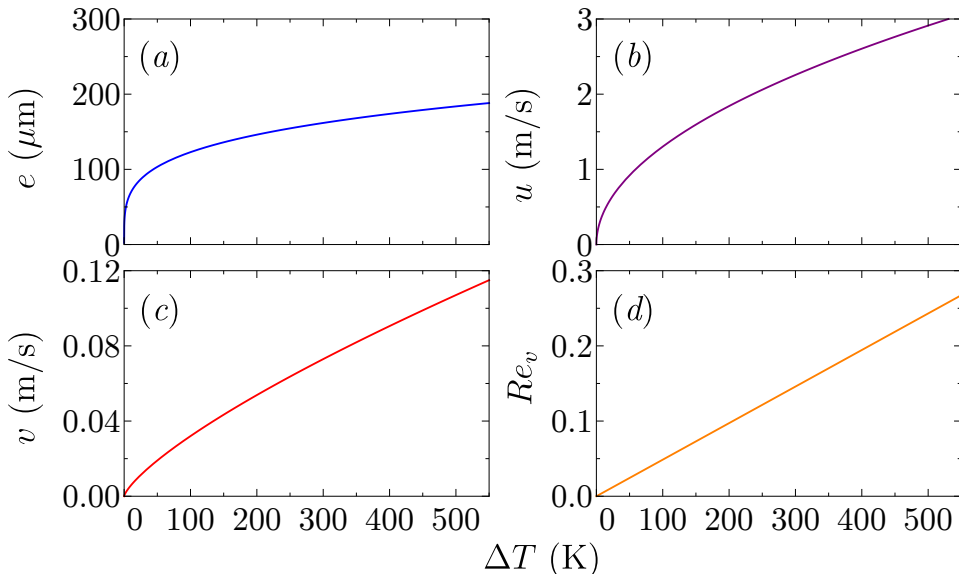


FIGURE 12. (Color online) Dependence of vapor film thickness (a), radial velocity (b), vertical velocity (c), and the Reynolds number in the vapor (d) on temperature difference  $\Delta T$ , respectively.

video frame rate (500-1000 Hz), and the maximum spatial frequency was set by half the camera magnification (132 px/cm).

We observed a sharp peak in the measured Fourier spectrum for all the analyzed video sequences. In figures 13(a) and 13(b) (8-mode, acetone), this peak is located at a capillary wave frequency  $f_c \approx 24$  Hz and within a range of wave numbers,  $k_c = 2\pi/\lambda_c$ , from  $7 \text{ cm}^{-1}$  to  $12 \text{ cm}^{-1}$ , where  $\lambda_c$  is the wavelength of the capillary waves. Figures 13(c) and 13(d) show the capillary waves beneath a 11-mode Leidenfrost ethanol drop and a sharp peak at a capillary wave frequency  $f_c \approx 25$  Hz with  $k_c \approx 7\text{-}10 \text{ cm}^{-1}$ . Similarly, for the capillary waves beneath a 12-mode Leidenfrost ethanol drop (figure 13(e)), a sharp peak exists at  $f_c \approx 27$  Hz and  $k_c \approx 10\text{-}11 \text{ cm}^{-1}$  as shown in figure 13(f). These frequencies show excellent agreement with the corresponding typical pressure oscillation frequencies measured in the vapor layer of star-shaped Leidenfrost ethanol and acetone drops (see figure 9c).

It is well-known that capillary waves can be generated at a liquid-vapor interface due to a strong shear stress in the vapor (Miles 1957; Zhang 1995; Paquier *et al.* 2015; Zeisel *et al.* 2008; Chang & Demekhin 2002). A similar mechanism underlies the Kelvin-Helmholtz instability, however, the intermediate Reynolds number in the Leidenfrost vapor layer complicates the analysis. Nevertheless, we can estimate the strength of this shear stress. Typically, the “friction velocity” is generally used to measure the strength of shear, which is defined as  $u_* = \sqrt{\tau/\rho_v}$ , where  $\tau$  is the shear stress at the liquid-vapor interface. The maximum shear stress at the interface is:

$$\tau = \frac{6\eta_v u}{e}, \quad (3.27)$$

assuming a parabolic-flow profile in the vapor layer with mean velocity  $u$  near the edge of the drop. Using water as an example, and plugging (3.24) and (3.26) and the value of  $\eta_v$  of water vapor into (3.27) yields  $u_* \approx 2$  m/s. This friction velocity is quite strong and

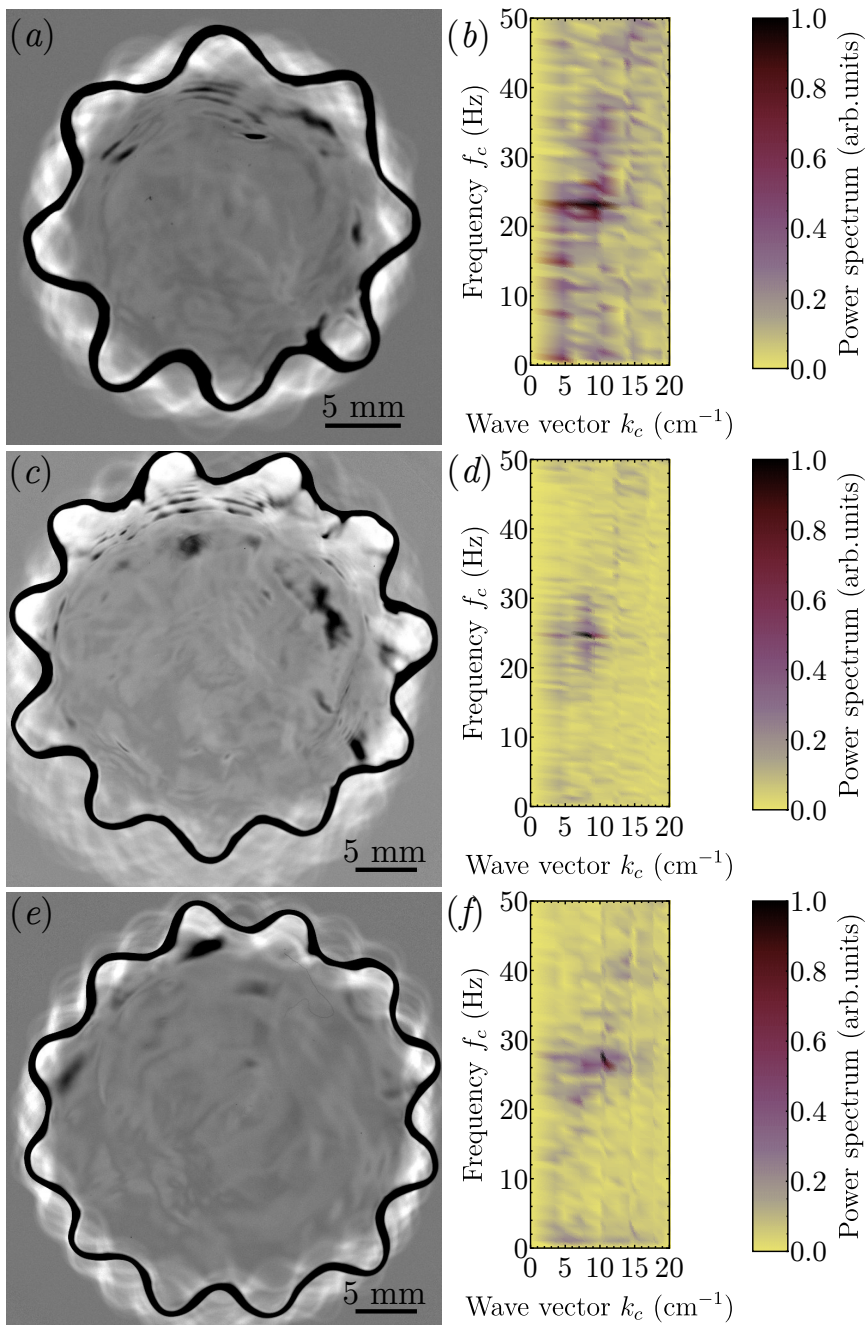


FIGURE 13. (Color online) (a) (c) and (e) show the capillary waves imaged beneath 8-mode acetone drop, 11-mode ethanol drop and 12-mode ethanol drop, respectively. (b), (d) and (f) represent the corresponding Fourier power spectra of the capillary waves shown in (a), (c), and (e), respectively. The images of capillary waves were enhanced for visibility, as described in the text.

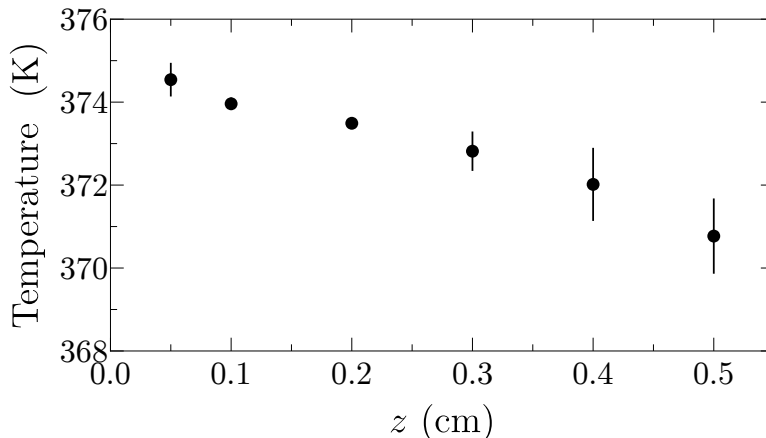


FIGURE 14. (Color online) The temperature profile of a large Leidenfrost water drop with the volume of  $10^{-6}$  m<sup>3</sup>. The error bars come from the standard deviations of multiple measurements.

sufficient to lead to the growth of unstable modes with wavelengths of millimeter scale (Zhang 1995; Zeisel *et al.* 2008).

The general dispersion relation of gravity-capillary waves with a dense upper-layer is:

$$f_c = \frac{1}{2\pi} \sqrt{\left(-gk_c + \frac{\gamma k_c^3}{\rho}\right) \tanh(k_c h)}, \quad (3.28)$$

where  $k_c = 2\pi/\lambda_c$ , and  $h \approx 2l_c$  is the thickness of the drop. For simplicity, we have assumed that the normal velocity is zero at the upper surface of the drop. For a large Leidenfrost water drop whose characteristic pressure oscillation frequency in the vapor layer is  $f_p \approx 26$  Hz (see figure 7), the corresponding capillary wavelength is calculated to be  $\lambda_c \approx 3.03l_c$ , so that  $k_c \approx 8.3$  cm<sup>-1</sup> (Ma *et al.* 2017). Similarly, for the Leidenfrost acetone and ethanol drops shown in figures 13(a), 13(c), and 13(e), the corresponding  $k_c \approx 13$  cm<sup>-1</sup>, which is slightly larger than the positions of the peaks indicated in figures 13(b), 13(d), and 13(f), where  $\lambda_c \approx 4l_c$ . The agreement between the estimate for  $k_c$  and the measurements shown in figure 13 is good considering the simplicity of (3.28), which is derived using an inviscid, semi-infinite flow in both phases.

The capillary-wave origin for the star-shaped oscillations also agrees with the minimum size of the  $n = 2$  mode. More specifically, the radius we measured in our experiments is  $R$  rather than  $R_{\text{neck}}$  as illustrated in figure 11. The relationship between these two lengths is  $R = R_{\text{neck}} + 0.53l_c$  (Snoeijer *et al.* 2009; Burton *et al.* 2012). Thus, the minimum drop size required to fit one capillary wavelength beneath the drop is  $2R_{\text{neck}} \approx \lambda_c$ . Using  $\lambda_c \approx 3.03l_c$  from above, we find that the radius of an  $n = 2$  mode drop should be  $R \approx 2.05l_c$ . This is in good agreement with figure 9(a), which shows  $R/l_c$  is slightly less than 2 for the smallest drops. Taken together, this analysis suggests a purely hydrodynamic origin for the star oscillations based on capillary waves generated by a strong shear stress in the rapidly-flowing vapor beneath the drop.

### 3.7. Thermal effects

In the Leidenfrost effect, thermal energy is transferred from the substrate to the drop, inducing evaporation and enabling the sustained star-shaped oscillations. Here we consider the role of thermal effects, such as convection in the liquid, which may play a role in the star oscillations. At sufficiently large temperature gradients in liquid

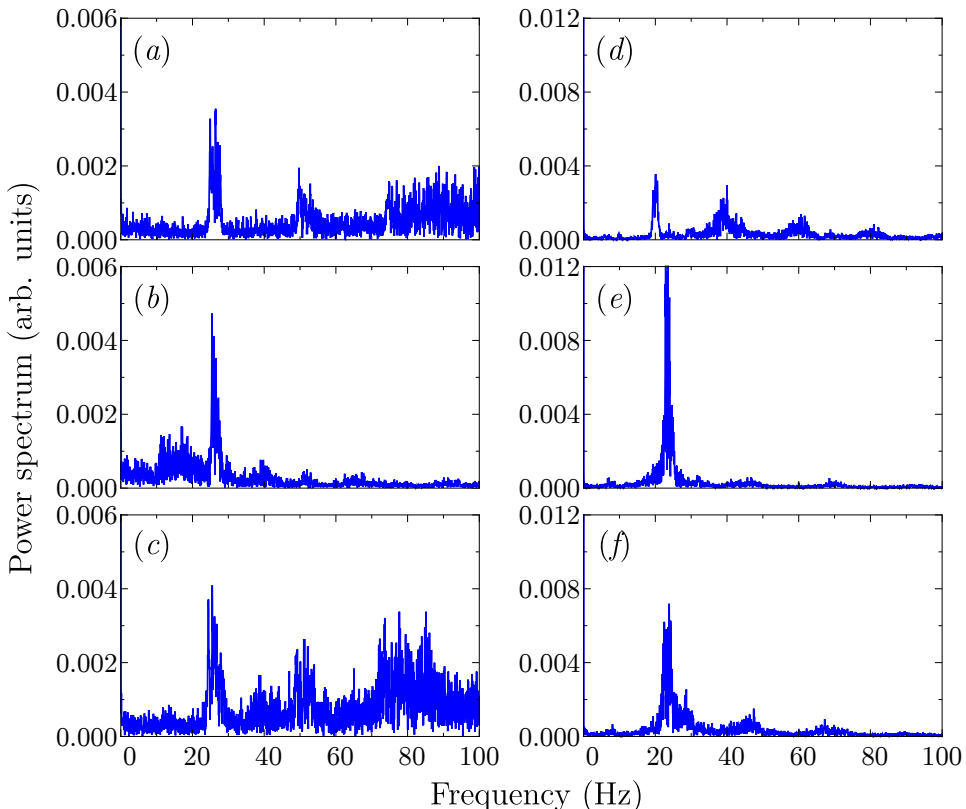


FIGURE 15. (Color online) Fourier power spectra of the pressure variations in the vapor layer at different environment temperature  $T_1$ . (a), (b) and (c) represent pressure variations of a 4-mode Leidenfrost water drop at  $T_1 \approx 367$  K, 483 K, and 623 K, respectively. (d), (e) and (f) represent pressure variations of a 5-mode Leidenfrost water drop at  $T_1 \approx 367$  K, 483 K, and 623 K, respectively. All of the data shown here was obtained at the same scanning rate within the same time interval, 20 s.

layers, convective structures can develop with well-defined length scales. A well-known example is Bénard-Marangoni convection, where hexagonal patterns are generated in a thin layer of liquid when heated from the bottom (Bénard 1901; Rayleigh 1916). The convection pattern is strongly affected by the variation of surface tension with temperature (Marangoni 1871; Schatz & Neitzel 2001; Maroto *et al.* 2007). Given that our data collapses when scaled by the capillary length of the liquid (figure 9), this particular type of convection may be important for Leidenfrost drops since the capillary length also appears in the length scale which characterizes the size of the convective patterns.

Generally, the Marangoni number,  $Ma$ , and Rayleigh number,  $Ra$ , are used to characterize Bénard-Marangoni convection. These dimensionless numbers are defined as:

$$Ma = \frac{(\partial\gamma/\partial T) \delta Th}{\nu_l \rho D_l}, \quad (3.29)$$

$$Ra = \frac{g \alpha \delta T h^3}{\nu_l D_l}. \quad (3.30)$$

These numbers characterize the strengths of thermocapillary and buoyancy effects, respectively. Additionally, the ratio of thermal conduction inside the liquid to the con-

Symbol	Quantity	Value
$\nu_l$	liquid kinematic viscosity	$2.94 \times 10^{-7} \text{ m}^2/\text{s}$
$D_l$	liquid thermal diffusivity	$1.743 \times 10^{-7} \text{ m}^2/\text{s}$
$\alpha$	thermal expansion coefficient	$7.52 \times 10^{-4} /\text{K}$
$\kappa_l$	liquid thermal conductivity	$3.2 \times 10^{-2} \text{ W/m/K}$
$h$	drop thickness	0.005 m
$\delta T$	temperature difference	$T_{\text{hot}} - T_{\text{cold}}$
$\beta$	heat transfer coefficient	depends on $\delta T$
$\partial\gamma/\partial T$	surface tension gradient	$1.46 \times 10^{-4} \text{ N/m/K}$
$T_1$	surface temperature	$>367 \text{ K}$

TABLE 2. Physical properties of water at the boiling points (Lemmon *et al.* 2011).

duction at the liquid-vapor interface is characterized by the Biot number:

$$Bi = \frac{\beta h}{\kappa_l} = \frac{T_{\text{hot}} - T_{\text{cold}}}{T_{\text{cold}} - T_1}, \quad (3.31)$$

The definitions of the symbols in  $Ma$ ,  $Ra$ , and  $Bi$  are listed in table 2, as well as their values for water at the boiling point.

Figure 14 shows the temperature profile of a large Leidenfrost water drop levitating on its vapor layer with  $T_s = 673 \text{ K}$ , in which the substrate surface is defined as  $z = 0$ . The temperature was measured with a fine-point thermocouple, as described in §2. We define the temperatures of the bottom and top surfaces of the drop as  $T_{\text{hot}}$  and  $T_{\text{cold}}$ , respectively, and the temperature of the position which is slightly above the top surface of the drop is denoted as the environment temperature,  $T_1$ , as shown in figure 11. From figure 14 we can obtain  $\delta T = T_{\text{hot}} - T_{\text{cold}} \approx 3.8 \text{ K}$ , the environment temperature measured to be  $T_1 = 367 \text{ K}$ , thus we can calculate  $Ma \sim 2 \times 10^5$ ,  $Ra \sim 7 \times 10^4$ , and  $Bi \approx 1.1$ . Both the values of  $Ma$  and  $Ra$  are much larger than their critical values, which are typically of order 100 for the initiation of convective instability (Maroto *et al.* 2007; Leal 2007). Thus it is possible that thermal convection plays a role in initiating the star-shaped oscillations. In this case, one may expect the star-shaped wavelength,  $\lambda_a$ , to be related to the critical wavelength of the convective instability. This critical wavelength depends on the Biot number. We implemented a qualitative test for this dependence by wrapping aluminum foil around the substrate and Leidenfrost drop, which dramatically increased the environment temperature,  $T_1$ , near the top of drop.

Figures 15(a) and 15(d) show Fourier power spectra of the pressure oscillations in the vapor layer of Leidenfrost water drops during  $n = 4$  and  $n = 5$  oscillations at  $T_1 \approx 367 \text{ K}$ , respectively. Figures 15(b) and 15(e) are the spectra of pressure oscillations during  $n = 4$  and  $n = 5$  oscillations at  $T_1 \approx 483 \text{ K}$ , respectively. Finally, figures 15(c) and 15(f) represent the same modes at  $T_1 = 623 \text{ K}$ . For  $T_1 = 483 \text{ K}$  and  $623 \text{ K}$ , the direction of heat transfer at the upper surface of the drop has been reversed; energy is added to the drop. Overall, dramatically increasing the surrounding temperature affects the appearance of higher harmonics in the spectra. The behavior is non-monotonic, and is likely due to the highly nonequilibrium conditions (high evaporation rate) induced by the high temperatures of the substrate ( $T_s$ ) and environment ( $T_1$ ). A more detailed understanding of the pressure oscillation spectra is left for future studies. Nevertheless, the position of the main peak in the spectra is independent of  $T_1$ , indicating that convection and the

details of thermal transport in Leidenfrost drops play a secondary role in the star-shaped oscillations.

#### 4. Conclusion and outlook

Both large and small Leidenfrost drops display self-organized oscillations due to the constant input of thermal energy and continuous evaporation and flow beneath the drop. Here we have focused on radial oscillations (i.e. “breathing” mode) of small Leidenfrost drops, and the large-amplitude, star-shaped oscillations that appear in large Leidenfrost drops. We have characterized the number of observed modes for various volatile liquids, the frequency and wavelength of the oscillations, and the pressure variations in the vapor layer beneath the drops. The number of observed modes is sensitive to the properties of the liquid (see table 1), i.e. the star-shaped oscillations of smaller Leidenfrost drops are dissipated by the liquid viscosity, which sets the minimum oscillation mode number  $n_{min}$  that can be observed in experiment. The relationship between the frequency and wavelength agrees very well the quasi-two-dimensional theory proposed by [Yoshiyasu \*et al.\* \(1996\)](#). The dominant frequency associated with the pressure oscillations is approximately twice the drop oscillation frequency, consistent with a parametric forcing mechanism for the star oscillations.

One of the main findings of our work is identifying the underlying cause of the pressure oscillations. By imaging the liquid-vapor interface from below the drop, and using a simplified model for the flow in the thin vapor layer, we conclude that capillary waves of a characteristic wavelength,  $\lambda_c \approx 4l_c$ , lead to pressure oscillations at the experimentally measured frequency. The flow in the vapor layer is quite rapid. Near the edge of the drop, the mean radial velocity can reach 1-2 m/s or more. In the small gap ( $\sim 100 \mu\text{m}$ ) between the liquid and the solid surface, this flow applies a large shear stress to the liquid-vapor interface, and can easily excite capillary waves with millimeter-scale wavelengths. The dispersion relation for the capillary waves then leads to a characteristic frequency for the pressure oscillations, which in turn parametrically drive the star-shaped oscillations. Furthermore, although the vapor flow is inherently driven by evaporation and heat transfer, the substrate and surrounding temperature have little effect on the dominant frequency and wavelength of the oscillations, suggesting they are purely hydrodynamic in origin.

Although the work presented here has focused mostly on the origin of star-shaped oscillations, the coupling of the flow in the vapor layer and the liquid-vapor interface underlies a rich spectrum of dynamical phenomena observed in both Leidenfrost liquid layers and drops. In particular, of key interest is understanding the failure of the Leidenfrost vapor layer which can lead to explosive boiling. If the observed capillary waves beneath the drop act as the precipitant to vapor-layer failure, then it is possible that geometrical tailoring of the surface to be commensurate with  $\lambda_c$  may inhibit the generation of capillary waves. In addition, patterned, ratchet-shaped substrates with with wavelengths  $\approx 1\text{-}3 \text{ mm}$  are known to induce propulsion of small Leidenfrost drops ([Cousins \*et al.\* 2012](#); [Linke \*et al.\* 2006](#); [Lagubeau \*et al.\* 2011](#)), however, less is known about transport of large quantities of liquid, and the dependence on the wavelength of the surface patterns. We leave these questions open to future experiments. More generally, our results may offer insight into the direct control of oscillations in levitated drops in many other systems ([Haumesser \*et al.\* 2002](#); [Duchemin \*et al.\* 2005](#); [Paradis & Ishikawa 2005](#); [Ishikawa \*et al.\* 2006](#); [Lister \*et al.\* 2008](#); [Langstaff \*et al.\* 2013](#)), for example, precise control is crucial when levitating high-temperature or harmful liquids using a gas film. We also expect our results to enhance the understanding of dynamics that couple a



thin, supporting gas film, a liquid interface, and a solid surface, a scenario which occurs through forced wetting and gas entrainment in liquid coating (Xu *et al.* 2005; Driscoll & Nagel 2011; Marchand *et al.* 2012; Kolinski *et al.* 2012; Liu *et al.* 2013, 2015).

## 5. Acknowledgements

We thank Tom Caswell for providing the experimental data related to the breathing mode of Leidenfrost drops, and Juan-José Liétor-Santos for helpful discussions. This work was supported by the National Science Foundation through grant NSF DMR-1455086.

## REFERENCES

- ABDELAZIZ, R., DISCI-ZAYED, D., HEDAYATI, M. K., PÖHLS, J-H, ZILLOHU, A. U., ERKARTAL, B., CHAKRAVADHANULA, V. S. K., DUPPEL, V., KIENLE, L. & ELBAHRI, M. 2013 Green chemistry and nanofabrication in a levitated Leidenfrost drop. *Nat. Commun.* **4**, 2400.
- ADACHI, K. & TAKAKI, R. 1984 Vibration of a flattened drop. I. Observation. *J. Phys. Soc. Jpn.* **53**, 4184–4191.
- BAIN, RYAN M., PULLIAM, C. J., THERY, F. & COOKS, R. G. 2016 Accelerated chemical reactions and organic synthesis in Leidenfrost droplets. *Angew. Chem. Int. Ed.* **55**, 10478–10482.
- BECKER, E., HILLER, W. J. & KOWALEWSKI, T. A. 1991 Experimental and theoretical investigation of large-amplitude oscillations of liquid droplets. *J. Fluid Mech.* **231**, 189–210.
- BÉNARD, H. 1901 Les tourbillons cellulaires dans une nappe liquide.—Méthodes optiques d’observation et d’enregistrement. *Journal de Physique Théorique et Appliquée* **10**, 254–266.
- BERNARDIN, J. D. & MUDAWAR, I. 1999 The Leidenfrost point: experimental study and assessment of existing models. *J. Heat Transfer.* **121**, 894–903.
- BIANCE, A-L, CHEVY, F., CLANET, C., LAGUBEAU, G. & QUÉRÉ, D. 2006 On the elasticity of an inertial liquid shock. *J. Fluid Mech.* **554**, 47–66.
- BIANCE, A-L, CLANET, C. & QUÉRÉ, D. 2003 Leidenfrost drops. *Phys. Fluids* **15**, 1632–1637.
- BOUWHUIS, W., WINKELS, K. G., PETERS, I. R., BRUNET, P., VAN DER MEER, D. & SNOEIJER, J. H. 2013 Oscillating and star-shaped drops levitated by an airflow. *Phys. Rev. E* **88**, 023017.
- BRUNET, P. & SNOEIJER, J. H. 2011 Star-drops formed by periodic excitation and on an air cushion—A short review. *Eur. Phys. J. Spec. Top.* **192**, 207–226.
- BURTON, J. C., HUISMAN, F. M., ALISON, P., ROGERSON, D. & TABOREK, P. 2010 Experimental and numerical investigation of the equilibrium geometry of liquid lenses. *Langmuir* **26**, 15316–15324.
- BURTON, J. C., SHARPE, A. L., VAN DER VEEN, R. C. A., FRANCO, A. & NAGEL, S. R. 2012 Geometry of the vapor layer under a Leidenfrost drop. *Phys. Rev. Lett.* **109**, 074301.
- CASTANET, G., CABALLINA, O. & LEMOINE, F. 2015 Drop spreading at the impact in the Leidenfrost boiling. *Phys. Fluids* **27**, 063302.
- CASWELL, T. A. 2014 Dynamics of the vapor layer below a Leidenfrost drop. *Phys. Rev. E* **90**, 013014.
- CHANG, H.-H. & DEMEKHIN, E. A. 2002 *Complex wave dynamics on thin films*. Elsevier.
- COUSINS, T. R., GOLDSTEIN, R. E., JAWORSKI, J. W. & PESCI, A. I. 2012 A ratchet trap for Leidenfrost drops. *J. Fluid Mech.* **696**, 215–227.
- DRISCOLL, M. M. & NAGEL, S. R. 2011 Ultrafast interference imaging of air in splashing dynamics. *Phys. Rev. Lett.* **107**, 154502.
- DUCHEMIN, L., LISTER, J. R. & LANGE, U. 2005 Static shapes of levitated viscous drops. *J. Fluid Mech.* **533**, 161–170.
- DUPEUX, G., LE MERRER, M., CLANET, C. & QUÉRÉ, D. 2011a Trapping Leidenfrost drops with crenulations. *Phys. Rev. Lett.* **107**, 114503.
- DUPEUX, G., LE MERRER, M., LAGUBEAU, G., CLANET, C., HARDT, S. & QUÉRÉ, D. 2011b Viscous mechanism for Leidenfrost propulsion on a ratchet. *EPL* **96**, 58001.

- HAUMESSER, P-H, BANCILLON, J., DANIEL, M., PEREZ, M. & GARANDET, J-P 2002 High-temperature contactless viscosity measurements by the gas-film levitation technique: Application to oxide and metallic glasses. *Rev. Sci. Instr.* **73**, 3275–3285.
- HIDALGO-CABALLERO, S., ESCOBAR-ORTEGA, Y. & PACHECO-VÁZQUEZ, F. 2016 Leidenfrost phenomenon on conical surfaces. *Phys. Rev. Fluids* **1**, 051902.
- HOLTER, N. J. & GLASSCOCK, W. R. 1952 Vibrations of evaporating liquid drops. *J. Acoust. Soc. Am.* **24**, 682–686.
- ISHIKAWA, T., YU, J. & PARADIS, P-F 2006 Noncontact surface tension and viscosity measurements of molten oxides with a pressurized hybrid electrostatic-aerodynamic levitator. *Rev. Sci. Instr.* **77**, 053901.
- KADOTA, T., TANAKA, H., SEGAWA, D., NAKAYA, S. & YAMASAKI, H. 2007 Microexplosion of an emulsion droplet during Leidenfrost burning. *Proc. Combust. Inst.* **31**, 2125–2131.
- KOLINSKI, J. M., RUBINSTEIN, S. M., MANDRE, S., BRENNER, M. P., WEITZ, D. A. & MAHADEVAN, L. 2012 Skating on a film of air: drops impacting on a surface. *Phys. Rev. Lett.* **108**, 074503.
- KUMAR, K. & TUCKERMAN, L. S. 1994 Parametric instability of the interface between two fluids. *J. Fluid Mech.* **279**, 49–68.
- LAGUBEAU, G., LE MERRER, M., CLANET, C. & QUÉRÉ, D. 2011 Leidenfrost on a ratchet. *Nat. Phys.* **7**, 395.
- LANGSTAFF, D., GUNN, M., GREAVES, G. N., MARSING, A. & KARGL, F. 2013 Aerodynamic levitator furnace for measuring thermophysical properties of refractory liquids. *Rev. Sci. Instr.* **84**, 124901.
- LEAL, L. G. 2007 *Advanced transport phenomena: fluid mechanics and convective transport processes*. Cambridge University Press.
- LEIDENFROST, J. G. 1756 *De aquae communis nonnullis qualitibus tractatus*. Ovenius.
- LEMMON, E. W., MCLINDEN, M. O., FRIEND, D. G., LINSTROM, P. J. & MALLARD, W. G. 2011 NIST chemistry WebBook, Nist standard reference database number 69. (*National Institute of Standards and Technology, Gaithersburg, MD, 2011*), <http://webbook.nist.gov>
- LI, J., HOU, Y., LIU, Y., HAO, C., LI, M., CHAUDHURY, M. K., YAO, S. & WANG, Z. 2016 Directional transport of high-temperature Janus droplets mediated by structural topography. *Nat. Phys.* **12**, 606.
- LINKE, H., ALEMÁN, B. J., MELING, L. D., TAORMINA, M. J., FRANCIS, M. J., DOW-HYGELUND, C. C., NARAYANAN, V., TAYLOR, R. P. & STOUT, A. 2006 Self-propelled Leidenfrost droplets. *Phys. Rev. Lett.* **96**, 154502.
- LISTER, J. R., THOMPSON, A. B., PERRIOT, A. & DUCHEMIN, L. 2008 Shape and stability of axisymmetric levitated viscous drops. *J. Fluid Mech.* **617**, 167–185.
- LIU, Y., TAN, P. & XU, L. 2013 Compressible air entrapment in high-speed drop impacts on solid surfaces. *J. Fluid Mech.* **716**, R9.
- LIU, Y., TAN, P. & XU, L. 2015 Kelvin-Helmholtz instability in an ultrathin air film causes drop splashing on smooth surfaces. *Proc. Natl. Acad. Sci. U.S.A.* **112**, 3280–3284.
- MA, X., LIÉTOR-SANTOS, J-J & BURTON, J. C. 2015 The many faces of a Leidenfrost drop. *Phys. Fluids* **27**, 091109.
- MA, X., LIÉTOR-SANTOS, J-J & BURTON, J. C. 2017 Star-shaped oscillations of Leidenfrost drops. *Phys. Rev. Fluids* **2**, 031602.
- MAMPALLIL, D., ERAL, H. B., STAIUCU, A., MUGELE, F. & VAN DEN ENDE, D. 2013 Electrowetting-driven oscillating drops sandwiched between two substrates. *Phys. Rev. E* **88**, 053015.
- MAQUET, L., BRANDENBOURGER, M., SOBAC, B., BIANCE, A-L, COLINET, P. & DORBOLO, S. 2015 Leidenfrost drops: Effect of gravity. *EPL* **110**, 24001.
- MAQUET, L., SOBAC, B., DARBOIS-TEXIER, B., DUCHESNE, A., BRANDENBOURGER, M., REDNIKOV, A., COLINET, P. & DORBOLO, S. 2016 Leidenfrost drops on a heated liquid pool. *Phys. Rev. Fluids* **1**, 053902.
- MARANGONI, C. 1871 Über die Ausbreitung der Tropfen einer Flüssigkeit auf der Oberfläche einer anderen. *Ann. Phys.* **219**, 337–354.
- MARCHAND, A., CHAN, T. S., SNOELJER, J. H. & ANDREOTTI, B. 2012 Air entrainment by contact lines of a solid plate plunged into a viscous fluid. *Phys. Rev. Lett.* **108**, 204501.

- MAROTO, J. A., PÉREZ-MUNUZURI, V. & ROMERO-CANO, M. S. 2007 Introductory analysis of Bénard–Marangoni convection. *Eur. J. Phys.* **28**, 311.
- MILES, J. & HENDERSON, D. 1990 Parametrically forced surface waves. *Annu. Rev. Fluid Mech.* **22**, 143–165.
- MILES, J. W. 1957 On the generation of surface waves by shear flows. *J. Fluid Mech.* **3**, 185–204.
- MYERS, T. G. & CHARPIN, J. P. F. 2009 A mathematical model of the Leidenfrost effect on an axisymmetric droplet. *Phys. Fluids* **21**, 063101.
- NOBLIN, X., BUGUIN, A. & BROCHARD-WYART, F. 2005 Triplon modes of puddles. *Phys. Rev. Lett.* **94**, 166102.
- NOBLIN, X., BUGUIN, A. & BROCHARD-WYART, F. 2009 Vibrations of sessile drops. *Eur. Phys. J. Spec. Top.* **166**, 7–10.
- PAQUIER, A., MOISY, F. & RABAUD, M. 2015 Surface deformations and wave generation by wind blowing over a viscous liquid. *Phys. Fluids* **27**, 122103.
- PARADIS, P-F & ISHIKAWA, T. 2005 Surface tension and viscosity measurements of liquid and undercooled alumina by containerless techniques. *Jpn. J. Appl. Phys.* **44**, 5082.
- POMEAU, Y., LE BERRE, M., CELESTINI, F. & FRISCH, T. 2012 The Leidenfrost effect: From quasi-spherical droplets to puddles. *C. R. Mecanique* **340**, 867–881.
- QUÉRÉ, D. 2013 Leidenfrost dynamics. *Annu. Rev. Fluid Mech.* **45**, 197–215.
- RAUX, P. S., DUPEUX, G., CLANET, C. & QUÉRÉ, D. 2015 Successive instabilities of confined Leidenfrost puddles. *EPL* **112**, 26002.
- RAYLEIGH, LORD 1879 On the capillary phenomena of jets. *Proc. R. Soc. London* **29**, 71–97.
- RAYLEIGH, L. 1916 LIX. On convection currents in a horizontal layer of fluid, when the higher temperature is on the under side. *Philos. Mag.* **32**, 529–546.
- SCHATZ, M. F. & NEITZEL, G. P. 2001 Experiments on thermocapillary instabilities. *Annu. Rev. Fluid Mech.* **33**, 93–127.
- SHAHRIARI, A., WURZ, J. & BAHADUR, V. 2014 Heat transfer enhancement accompanying Leidenfrost state suppression at ultrahigh temperatures. *Langmuir* **30**, 12074–12081.
- SHEN, C. L., XIE, W. J. & WEI, B. 2010a Parametric resonance in acoustically levitated water drops. *Phys. Rev. Lett. A* **374**, 2301–2304.
- SHEN, C. L., XIE, W. J. & WEI, B. 2010b Parametrically excited sectorial oscillation of liquid drops floating in ultrasound. *Phys. Rev. E* **81**, 046305.
- SHIROTA, M., VAN LIMBEEK, M. A. J., SUN, C., PROSPERETTI, A. & LOHSE, D. 2016 Dynamic Leidenfrost effect: relevant time and length scales. *Phys. Rev. Lett.* **116**, 064501.
- SMITH, W. R. 2010 Modulation equations for strongly nonlinear oscillations of an incompressible viscous drop. *J. Fluid Mech.* **654**, 141–159.
- SNEZHKO, A., JACOB, E. B. & ARANSON, I. S. 2008 Pulsating–gliding transition in the dynamics of levitating liquid nitrogen droplets. *New J. Phys.* **10**, 043034.
- SNOELJER, J. H., BRUNET, P. & EGGERS, J. 2009 Maximum size of drops levitated by an air cushion. *Phys. Rev. E* **79**, 036307.
- SOBAC, B., REDNIKOV, A., DORBOLO, S. & COLINET, P. 2014 Leidenfrost effect: Accurate drop shape modeling and refined scaling laws. *Phys. Rev. E* **90**, 053011.
- SOBAC, B., REDNIKOV, A., DORBOLO, S. & COLINET, P. 2017 Self-propelled Leidenfrost drops on a thermal gradient: A theoretical study. *Phys. Fluids* **29**, 082101.
- SOTO, D., LAGUBEAU, G., CLANET, C. & QUÉRÉ, D. 2016 Surfing on a herringbone. *Phys. Rev. Fluids* p. 013902.
- STRIER, D. E., DUARTE, A. A., FERRARI, H. & MINDLIN, G. B. 2000 Nitrogen stars: morphogenesis of a liquid drop. *Physica A* **283**, 261–266.
- TAKAKI, R. & ADACHI, K. 1985 Vibration of a flattened drop. II. Normal mode analysis. *J. Phys. Soc. Jpn.* **54**, 2462–2469.
- TALARI, V., BEHAR, P., LU, Y., HARYADI, E. & LIU, D. 2018 Leidenfrost drops on micro/nanostructured surfaces. *Front. Energy* pp. 1–21.
- TERWAGNE, D. & BUSH, J. W. M. 2011 Tibetan singing bowls. *Nonlinearity* **24**, R51.
- TOKUGAWA, N. & TAKAKI, R. 1994 Mechanism of self-induced vibration of a liquid drop based on the surface tension fluctuation. *J. Phys. Soc. Jpn.* **63**, 1758–1768.
- TRAN, T., STAAT, H. J. J., PROSPERETTI, A., SUN, C. & LOHSE, D. 2012 Drop impact on superheated surfaces. *Phys. Rev. Lett.* **108**, 036101.

- TRINH, P. H., KIM, H., HAMMOUD, N., HOWELL, P. D., CHAPMAN, S. J. & STONE, H. A. 2014 Curvature suppresses the Rayleigh-Taylor instability. *Phys. Fluids* **26**, 051704.
- VAKARELSKI, I. U., CHAN, D. Y. C. & THORODDSEN, S. T. 2014 Leidenfrost vapour layer moderation of the drag crisis and trajectories of superhydrophobic and hydrophilic spheres falling in water. *Soft Matter* **10**, 5662–5668.
- VAKARELSKI, I. U., MARSTON, J. O., CHAN, D. Y. C. & THORODDSEN, S. T. 2011 Drag reduction by Leidenfrost vapor layers. *Phys. Rev. Lett.* **106**, 214501.
- VAKARELSKI, I. U., PATANKAR, N. A., MARSTON, J. O., CHAN, D. Y. C. & THORODDSEN, S. T. 2012 Stabilization of Leidenfrost vapour layer by textured superhydrophobic surfaces. *Nature* **489**, 274.
- VAN DAM, H. 1992 Physics of nuclear reactor safety. *Rep. Prog. Phys.* **55**, 2025.
- WAITUKAITIS, S. R., ZUIDERWIJK, A., SOUSLOV, A., COULAIS, C. & VAN HECKE, M. 2017 Coupling the Leidenfrost effect and elastic deformations to power sustained bouncing. *Nat. Phys.* **13** (11), 1095.
- WONG, C. Y. H., ADDA-BEDIA, M. & VELLA, D. 2017 Non-wetting drops at liquid interfaces: from liquid marbles to Leidenfrost drops. *Soft matter* **13**, 5250–5260.
- XU, L., ZHANG, W. W. & NAGEL, S. R. 2005 Drop splashing on a dry smooth surface. *Phys. Rev. Lett.* **94**, 184505.
- XU, X. & QIAN, T. 2013 Hydrodynamics of Leidenfrost droplets in one-component fluids. *Phys. Rev. E* **87**, 043013.
- YOSHIYASU, N., MATSUDA, K. & TAKAKI, R. 1996 Self-induced vibration of a water drop placed on an oscillating plate. *J. Phys. Soc. Jpn.* **65**, 2068–2071.
- ZEISEL, A., STIASSNIE, M. & AGNON, Y. 2008 Viscous effects on wave generation by strong winds. *J. Fluid Mech.* **597**, 343–369.
- ZHANG, X. 1995 Capillary-gravity and capillary waves generated in a wind wave tank: observations and theories. *J. Fluid Mech.* **289**, 51.